ANL/NE-11-40

FY2011 Status Report on SN2ND Neutronics Solver Development

Nuclear Engineering Division

About Argonne National Laboratory

Argonne is a U.S. Department of Energy laboratory managed by UChicago Argonne, LLC under contract DE-AC02-06CH11357. The Laboratory's main facility is outside Chicago, at 9700 South Cass Avenue, Argonne, Illinois 60439. For information about Argonne, see http://www.anl.gov.

Availability of This Report

This report is available, at no cost, at http://www.osti.gov/bridge. It is also available on paper to the U.S. Department of Energy and its contractors, for a processing fee, from:

U.S. Department of Energy
Office of Scientific and Technical Information
P.O. Box 62
Oak Ridge, TN 37831-0062
phone (865) 576-8401
fax (865) 576-5728
reports@adonis.osti.gov

Disclaimer

This report was prepared as an account of work sponsored by an agency of the United States Government. Neither the United States Government nor any agency thereof, nor UChicago Argonne, LLC, nor any of their employees or officers, makes any warranty, express or implied, or assumes any legal liability or responsibility for the accuracy, completeness, or usefulness of any information, apparatus, product, or process disclosed, or represents that its use would not infringe privately owned rights. Reference herein to any specific commercial product, process, or service by trade name, trademark, manufacturer, or otherwise, does not necessarily constitute or imply its endorsement, recommendation, or favoring by the United States Government or any agency thereof. The views and opinions of document authors expressed herein do not necessarily state or reflect those of the United States Government or any agency thereof, Argonne National Laboratory, or UChicago Argonne, LLC.

ANL/NE-11-40

FY2011 Status Report on SN2ND Neutronics Solver Development

M. A. Smith, A. Mohamed, A. Marin-Lafleche, C. H. Lee, and W. S. Yang
Nuclear Engineering Division
Argonne National Laboratory

September 30, 2011

SUMMARY

A change in focus of NEAMS to a broader set of reactor types necessitated significant effort being diverted away from SN2ND development in FY2011. Nevertheless, significant gains were made with regard to building the new preconditioner and meeting the objectives of 1) parallelism in energy, 2) a spatial multigrid concept, 3) using S_N vector spaces to accommodate the adjoint and time dependent functionalities needed for NEAMS work, and 4) complete manuals and documentation. While the desired goal of an exportable SN2ND solver usable within the NEAMS community for neutronics analysis was not completed, we can be confident that this year's work puts the SN2ND solver well on its way to meeting that objective. It is important to note that SN2ND is just as capable as any other methodology for doing thermal reactor analysis, but the motivation to execute on smaller scale machines has initiated focused development on simplified treatments such as those proposed in the MOCARV tool.

All of the cited coding tasks were completed but not all are fully working (i.e. debugged). The spatial multigrid technique was by far the most time consuming part of the SN2ND development process. It required multiple new data structure concepts along with identifying the necessary changes in the vectors and their associated functions. Combining the spatial multigrid as part of a GMRES preconditioner operating on the full vector space, necessary for parallelization in energy, increased the complexity of that development. Research into spatial multigrid techniques for unstructured meshes, void treatments, and code optimization and acceleration are key development needs for SN2ND.

Similar to previous years, a considerable amount of effort was spent on validation work. Again we focused on fast reactor problems such as ZPR experiments and the MONJU reactor in Japan. Conventional drawer homogenized models and partially heterogeneous models were used on the ZPR calculations. The drawer homogenized models produced excellent results for both eigenvalue and foil measurements on four loadings of ZPR-6/7. The partially heterogeneous models of ZPR-6/7 also produced good results, but additional work is necessary to generate consistent effective cross section data. Calculations for MONJU were homogeneous and also gave excellent results.

Finally, mock-up heterogeneous calculations were setup and attempted to scope out the performance limitations of SN2ND on whole core heterogeneous calculations. Specifically, heterogeneous models of a PWR, a VHTR, and the MONJU reactor were created using anywhere from 2 group to 33 group cross section data. Meshes with greater than 100,000,000 vertices are necessary for accuracy and a specific non-scaling memory issue in PETSc restricted the SN2ND modeling (VHTR and PWR could not be solved). All of the calculations performed this year indicate that significant computational resources beyond those available today are required to obtain a high fidelity solution possible with SN2ND.

The future goals for SN2ND are to get the new version fully working, reliable in execution, and to have comparable performance to the old solver such that it can be released within the NEAMS community. After its export to RSICC, we will rely upon further preconditioner research to be done in collaboration with university partners and through the exascale hub activities. Some of that research will focus on making SN2ND applicable to thermal reactor problems, spatial multigrid, and void treatments.

TABLE OF CONTENTS

Summary i

Table of Contents iii

List of Figures iv

List of Tables iv

1 Introduction 5

2 Development Efforts on the SN2ND Solver 5

2.1 SN2ND Transport Discretization Review 6
2.2 SN2ND Transition to a GMRES Based Solution Algorithm 9
2.3 SN2ND Spatial Multigrid Preconditioning Scheme 11
2.4 Development of a Multi-grid Preconditioner 12
2.5 Implementation Concerns about Spatial Multigrid 15

3 SN2ND Validation Work 17

3.1 Homogenized Drawer Modeling of ZPR-6 Assembly 7 Experiment 17
3.2 Partially Heterogeneous Modeling of ZPR-6 Assembly 7 Experiment 22
3.3 Homogenized Assembly Modeling of the MONJU Fast Reactor 26
3.4 Fully Heterogeneous Modeling of Nuclear Reactors 30

4 Conclusions 33

5 References 35

LIST OF FIGURES

Figure 2.1 Serendipity (upper six) and Lagrangian (lower six) Quadrilaterals (left six) and their Tessellated Counterparts (right six) 15
Figure 2.2 Current Multigrid Steps Available in the new SN2ND Solver 15
Figure 2.3 Quadrilateral (left) and Triangularly Tessellated Quadrilateral (right) 16
Figure 3.1. ZPR-6/7 Geometry and Selected Flux Plots for Loading 106 18
Figure 3.2. ZPR-6/7 Description of Foil Types and Locations 20
Figure 3.3. Depiction of the Spatial Heterogeneity in the Stationary Matrix Half (Front Picture in Each Model) and Movable Matrix Half (Back Picture in Each Model) 23
Figure 3.4. Spatial Heterogeneity for each drawer 23
Figure 3.5. Finite Element Mesh per Hexagon for the SN2ND Models 26
Figure 3.6. Schematic of the MONJU Reactor Showing the Edit Line ED 28
Figure 3.7. Nine Group Flux Edits on the Selected Line ED in Figure 3.6. 28
Figure 3.8. PWR Finite Element Meshed Geometry. 30
Figure 3.9. VHTR Finite Element Meshed Geometry. 31
Figure 3.10. MONJU Finite Element Meshed Geometry 32
Figure 3.11. MONJU 3D Geometry and Flux and Power Solutions 33

LIST OF TABLES

Table 3.1. ZPR6-7 Loadings 104, 106, 120, and 132 Measured and Calculated Eigenvalues 19
Table 3.2. C/E Values in % Error for Normalized Foil Reaction Rates 21
Table 3.3. Comparison of C/E Values (% Error) for Normalized Foil Reaction Rates Determined with Cross Sections from One-Dimensional MC^2-3 and Two-Dimensional MCNP Calculations 22
Table 3.4. k_{eff} Space-Angle Convergence for the Four Heterogeneous Models of Loading 104 24
Table 3.5. Extrapolated k_{eff} results for ZPR6/7 Loading 104 25
Table 3.6. Loading 104 C/E Values in % Error for Normalized Foil Reaction Rates 25
Table 3.7. UNIC Space-Angle Mesh Refinement using 70 Group Cross Sections 27
Table 3.8. UNIC Space-Angle Mesh Refinement using 230 Group Cross Sections 27
Table 3.9. MONJU k_{eff} Results for Different Central Control Rod Configurations 29
Table 3.10. SN2ND and VARIANT Isothermal Temperature Coefficient for MONJU 29

1 Introduction

As part of the NEAMS activity in DOE, a fast reactor simulation program was launched in April 2007, termed SHARP [1]. The goal of SHARP was to develop a suite of modern simulation tools specifically for the analysis and design of sodium cooled fast reactors and has been extended to consider all reactor types of interest. The basic goal is to reduce the uncertainties and biases in various areas of reactor design activities by providing enhanced prediction capabilities. For the fast reactor component, a high-fidelity deterministic neutron transport code named UNIC [2-3] was started providing a common framework for fast reactor neutronics tools.

The application scope targeted for UNIC ranged from the homogenized assembly approaches prevalent in current reactor analysis methodologies to explicit geometry, time dependent transport calculations coupled to thermal-hydraulics and structural mechanics calculations for reactor accident simulations. The creation of a single solver that can perform all of these calculations and be competitive with the wide range of analysis tools already in use is somewhat formidable. Given the large assortment of transport solvers capable of treating the assembly homogenized, if not pin-cell homogenized geometry, the initial focus of UNIC was to create a single interface appropriate for the multi-physics (structural mechanics and thermal-hydraulics) coupling problems of immediate interest that are beyond the modeling capabilities of the existing tools.

Given the widened scope of reactor types and the differences associated with cross section processing [4,5], a single neutronics code is not practical and thus development on UNIC as a single entity has ended. Instead, the individual solvers developed thus far: SN2ND, PN2ND, MOCFE, and NODAL have been separated such that they can be incorporated in the specific end use reactor projects they are being developed for. Given that the analysis objectives for fast and thermal reactor systems are similar, we term the analysis usage of the different components as PROTEUS. In this report we discuss the development made to the SN2ND and the PROTEUS (MC^2-3 [5-6] + SN2ND) usage on modeling a ZPR experiment and the MONJU fast reactor.

This report is organized into three sections. Section 2 discusses the work carried out on improving the SN2ND solver algorithm which incorporates parallelism in energy and spatial multigrid concepts. Section 3 summarizes the validation calculations with PROTEUS on several fast reactor problems in addition to some full core heterogeneous models of thermal reactors. Section 4 discusses the ongoing effort to publicize the work being done at ANL for NEAMS.

2 Development Efforts on the SN2ND Solver

The SN2ND solver was originally started in the middle of FY2007. It can be safely stated to be the only successful solver created within UNIC with respect to massive parallelism and performance. The achievements of SN2ND were made possible by partitioning the space-angle system of equations over the available processors and utilizing established iterative solution techniques from the neutron transport community combined with the parallel algorithms in the PETSc toolbox [9]. Improvements were made in FY2009 and FY2010 with respect to performance and the stated goal in FY2010 was a complete rebuild of SN2ND including: 1) parallelism in energy, 2) a spatial multigrid concept 3) S_N vector spaces to

accommodate the adjoint and time dependent functionalities needed for NEAMS work, and 4) complete manuals and documentation. The obvious goal is an exportable product usable within the NEAMS community for neutronics analysis through RSICC [19].

2.1 SN2ND Transport Discretization Review

The desire to implement all of the stated features required significant changes in the setup of the SN2ND solver such that the FY2011 work was a "rewrite." To begin, we revisit the even- and odd-parity within-group transport equations

$$\hat{\Omega}\cdot\vec{\nabla}\psi_g^-(\vec{r},\hat{\Omega})+\Sigma_{t,g}(\vec{r})\psi_g^+(\vec{r},\hat{\Omega})=W_g^+(\vec{r},\hat{\Omega})+S_g^+(\vec{r},\hat{\Omega}) \tag{2.1}$$

$$\hat{\Omega}\cdot\vec{\nabla}\psi_g^+(\vec{r},\hat{\Omega})+\Sigma_{t,g}(\vec{r})\psi_g^-(\vec{r},\hat{\Omega})=W_g^-(\vec{r},\hat{\Omega})+S_g^-(\vec{r},\hat{\Omega}), \tag{2.2}$$

where $\psi_g^{\pm}(\vec{r},\hat{\Omega})$ is the even (+) and odd (-) parity flux, $W_g^{\pm}(\vec{r},\hat{\Omega})$ is the within-group scattering source, and $S_g^{\pm}(\vec{r},\hat{\Omega})$ is the out of group scattering and fission sources. The primary focus of the SN2ND derivation is to recast these two first-order equations into a second-order equation for the even-parity flux with the form [2]:

$$\mathrm{T}_e\left[\tilde{\psi}_{g,e}^+,\tilde{s}_{g,e}^{\pm}\right]=A_{g,e}\tilde{\psi}_{g,e}^+-\tilde{s}_{g,e}^+-\tilde{s}_{g,e}^-+BC_{g,e}. \tag{2.3}$$

Equation 2.3 is assembled over each finite element (e) in the domain and all angles in the cubature yielding a symmetric positive-definite coefficient matrix $A_{g,e}$ that is solvable using the efficient conjugate gradient (CG) algorithm as discussed previously [2].

Focusing on the impact of including parallelism in energy, we must expand the sources on the right hand side of equations 2.1 and 2.2 to show the group to group scattering sources

$$\hat{\Omega}\cdot\vec{\nabla}\psi_g^-(\vec{r},\hat{\Omega})+\Sigma_{t,g}(\vec{r})\psi_g^+(\vec{r},\hat{\Omega})=\sum_{g'}W_{gg'}^+(\vec{r},\hat{\Omega}\cdot\hat{\Omega}')\psi_{g'}^+(\vec{r},\hat{\Omega}')+Q_g^+(\vec{r},\hat{\Omega}) \tag{2.4}$$

$$\hat{\Omega}\cdot\vec{\nabla}\psi_g^+(\vec{r},\hat{\Omega})+\Sigma_{t,g}(\vec{r})\psi_g^-(\vec{r},\hat{\Omega})=\sum_{g'}W_{gg'}^-(\vec{r},\hat{\Omega}\cdot\hat{\Omega}')\psi_{g'}^-(\vec{r},\hat{\Omega}')+Q_g^-(\vec{r},\hat{\Omega}). \tag{2.5}$$

The second equation is solved for the odd-parity flux

$$\psi_g^-(\vec{r},\hat{\Omega})=-\frac{1}{\Sigma_{t,g}(\vec{r})}\hat{\Omega}\cdot\vec{\nabla}\psi_g^+(\vec{r},\hat{\Omega})+\frac{1}{\Sigma_{t,g}(\vec{r})}\left[\sum_{g'}W_{gg'}^-(\vec{r},\hat{\Omega}\cdot\hat{\Omega}')\psi_{g'}^-(\vec{r},\hat{\Omega}')+Q_g^-(\vec{r},\hat{\Omega})\right]. \tag{2.6}$$

Spatial weighting and integration yields

$$\psi_{g,e,n}^-=-\frac{\hat{\Omega}_{K,n}}{\Sigma_{t,g}}F^{-1}U_K\psi_{g,e,n}^++\frac{1}{\Sigma_{t,g}}\sum_{g'}Y_-(\hat{\Omega}_n)\sigma_{gg',e}^-\Phi_{g',e}^-+\frac{1}{\Sigma_{t,g}}Q_{g,n}^-. \tag{2.7}$$

Substitution into equation 2.4 followed by spatial weighting and integration gives

$$\begin{aligned}&\left[\sum_{K,L}\frac{\hat{\Omega}_{K,n}\hat{\Omega}_{L,n}}{\Sigma_{t,g,e}}P_{e,K,L}+\Sigma_{t,g,e}F_e+BC_{g,e,n}\right]\psi_{g,e,n}^+-\sum_{g'}Y_+(\hat{\Omega}_n)\sigma_{gg',e}^+F_e\,\Phi_{g',e}^+-F_e\,Q_{g,e,n}^+\\&-\sum_K\frac{\hat{\Omega}_{K,n}}{\Sigma_{t,g,e}}U_{e,K}^T\sum_{g'}Y_-(\hat{\Omega}_n)\sigma_{gg',e}^-\Phi_{g',e}^--\sum_K\frac{\hat{\Omega}_{K,n}}{\Sigma_{t,g,e}}U_{e,K}^TQ_{g,e,n}^-=0\end{aligned}, \tag{2.8}$$

$BC_{g,e,n}$ stands for the boundary condition modifications that are applied to each finite element in the domain. Equation 2.8 reduces to the form shown earlier in equation 2.3, but for energy parallelism we find

$$A_{g,e,n}\psi^{+}_{g,e,n} - \sum_{g',n'} W^{+}_{gg',e,n'} F_e \psi^{+}_{g',e,n,n'} + K_{g,e,n} \sum_{g',n'} W^{-}_{gg',e,n,n'} \psi^{-}_{g',e,n'} = F_e Q^{+}_{g,e,n} + K_{g,e,n} Q^{-}_{g,e,n}, \tag{2.9}$$

to be more convenient. In equation 2.9, we have defined

$$A_{g,e,n} = \sum_{K,L} \frac{\hat{\Omega}_{K,n}\hat{\Omega}_{L,n}}{\Sigma_{t,g,e}} P_{e,K,L} + \Sigma_{t,g,e} F_e + BC_{g,e,n}, \tag{2.10}$$

$$W^{\pm}_{gg',e,n,n'} = Y_{\pm}(\hat{\Omega}_n)\sigma^{\pm}_{gg',e} Y^{T}_{\pm}(\hat{\Omega}_{n'}) w_{n'}, \tag{2.11}$$

$$K_{g,e,n} = \sum_{K} \frac{\hat{\Omega}_{K,n}}{\Sigma_{t,g,e}} U^{T}_{e,K}, \tag{2.12}$$

The odd-parity transport equation, equation 2.6, can also be written in a discrete form

$$\psi^{-}_{g,e,n} = L_{g,e,n}\psi^{+}_{g,e,n} + \frac{1}{\Sigma_{t,g}} \sum_{g',n'} W^{-}_{gg',e,n,n'} \psi^{-}_{g',e,n'} + \frac{1}{\Sigma_{t,g}} Q^{-}_{g,n}. \tag{2.13}$$

$$L_{g,e,n} = \frac{\hat{\Omega}_{K,n}}{\Sigma_{t,g,e}} F_e^{-1} U^{T}_{e,K}, \tag{2.14}$$

Assembling the even-parity equation by direction we obtain

$$\begin{bmatrix} A_{g,e,1} - W^{+}_{gg,e,1,1}F_e & -W^{+}_{gg,e,1,N}F_e \\ -W^{+}_{gg,e,N,1}F_e & A_{g,e,N} - W^{+}_{gg,e,N,N}F_e \end{bmatrix} \begin{bmatrix} \psi^{+}_{g,e,1} \\ \psi^{+}_{g,e,N} \end{bmatrix} - \begin{bmatrix} K_{g,e,1}W^{-}_{gg,e,1,1} & K_{g,e,1}W^{-}_{gg,e,1,N} \\ K_{g,e,N}W^{-}_{gg,e,N,1} & K_{g,e,N}W^{-}_{gg,e,N,N} \end{bmatrix} \begin{bmatrix} \psi^{-}_{g,e,1} \\ \psi^{-}_{g,e,N} \end{bmatrix}$$

$$-\sum_{g'\neq g} \begin{bmatrix} W^{+}_{gg',e,1,1}F_e & W^{+}_{gg',e,1,N}F_e \\ W^{+}_{gg',e,N,1}F_e & W^{+}_{gg',e,N,N}F_e \end{bmatrix} \begin{bmatrix} \psi^{+}_{g',e,1} \\ \psi^{+}_{g',e,N} \end{bmatrix} - \sum_{g'\neq g} \begin{bmatrix} K_{g,e,1}W^{-}_{gg',e,1,1} & K_{g,e,1}W^{-}_{gg',e,1,N} \\ K_{g,e,N}W^{-}_{gg',e,N,1} & K_{g,e,N}W^{-}_{gg',e,N,N} \end{bmatrix} \begin{bmatrix} \psi^{-}_{g',e,1} \\ \psi^{-}_{g',e,N} \end{bmatrix}$$

$$= \begin{bmatrix} F_e & 0 \\ 0 & F_e \end{bmatrix} \begin{bmatrix} Q^{+}_{g,e,1} \\ Q^{+}_{g,e,N} \end{bmatrix} - \begin{bmatrix} K_{g,e,1} & 0 \\ 0 & K_{g,e,N} \end{bmatrix} \begin{bmatrix} Q^{-}_{g,e,1} \\ Q^{-}_{g,e,N} \end{bmatrix}$$

We write this compactly as

$$A^{++}_{gg,e}\psi^{+}_{g,e} + A^{+-}_{gg,e}\psi^{-}_{g,e} + \sum_{g'\neq g} A^{++}_{gg',e}\psi^{+}_{g',e} + \sum_{g'\neq g} A^{+-}_{gg',e}\psi^{-}_{g',e} = F_e Q^{+}_{g,e} + K_{g,e} Q^{-}_{g,e}, \tag{2.15}$$

$$A^{++}_{gg',e} = \delta_{gg'} \begin{bmatrix} A_{g,e,1} & 0 \\ 0 & A_{g,e,N} \end{bmatrix} - \begin{bmatrix} W^{+}_{gg',e,1,1} & W^{+}_{gg',e,1,N} \\ W^{+}_{gg',e,N,1} & W^{+}_{gg',e,N,N} \end{bmatrix} \begin{bmatrix} F_e & 0 \\ 0 & F_e \end{bmatrix}, \tag{2.16}$$

$$A^{+-}_{gg',e} = -\begin{bmatrix} K_{g,e,1} & 0 \\ 0 & K_{g,e,N} \end{bmatrix} \begin{bmatrix} W^{-}_{gg',e,1,1} & W^{-}_{gg',e,1,N} \\ W^{-}_{gg',e,N,1} & W^{-}_{gg',e,N,N} \end{bmatrix}. \tag{2.17}$$

Assembling the odd-parity equation by direction we have

$$\begin{bmatrix} I-\Sigma_{t,g}^{-1}W_{gg,e,1,1}^{-} & -\Sigma_{t,g}^{-1}W_{gg,e,1,N}^{-} \\ -\Sigma_{t,g}^{-1}W_{gg,e,N,1}^{-} & I-\Sigma_{t,g}^{-1}W_{gg,e,N,N}^{-} \end{bmatrix}\begin{bmatrix} \psi_{g,e,1}^{-} \\ \psi_{g,e,N}^{-} \end{bmatrix}+\sum_{g'\neq g}\begin{bmatrix} -\Sigma_{t,g}^{-1}W_{gg',e,1,1}^{-} & -\Sigma_{t,g}^{-1}W_{gg',e,1,N}^{-} \\ -\Sigma_{t,g}^{-1}W_{gg',e,N,1}^{-} & I-\Sigma_{t,g}^{-1}W_{gg',e,N,N}^{-} \end{bmatrix}\begin{bmatrix} \psi_{g',e,1}^{-} \\ \psi_{g',e,N}^{-} \end{bmatrix}$$
$$+\begin{bmatrix} L_{g,e,1} & 0 \\ 0 & L_{g,e,N} \end{bmatrix}\begin{bmatrix} \psi_{g,e,1}^{+} \\ \psi_{g,e,N}^{+} \end{bmatrix}=\Sigma_{t,g}^{-1}\begin{bmatrix} Q_{g,1}^{-} \\ Q_{g,N}^{-} \end{bmatrix}$$

which we can write compactly as

$$A_{gg,e}^{--}\psi_{g,e}^{-}+\sum_{g'\neq g}A_{gg',e}^{--}\psi_{g',e}^{-}+A_{gg,e}^{-+}\psi_{g,e}^{+}=\Sigma_{t,g}^{-1}Q_{g}^{-}, \tag{2.18}$$

$$A_{gg',e}^{--}=\delta_{g,g'}\begin{bmatrix} I & 0 \\ 0 & I \end{bmatrix}-\frac{1}{\Sigma_{t,g}}\begin{bmatrix} W_{gg,e,1,1}^{-} & W_{gg,e,1,N}^{-} \\ W_{gg,e,N,1}^{-} & W_{gg,e,N,N}^{-} \end{bmatrix}, \tag{2.19}$$

$$A_{gg',e}^{-+}=\begin{bmatrix} L_{g,e,1} & 0 \\ 0 & L_{g,e,N} \end{bmatrix}. \tag{2.20}$$

Partitioning equations 2.15 and 2.18 over a given group we can write

$$\begin{bmatrix} A_{gg,e}^{++} & A_{gg,e}^{+-} \\ A_{gg,e}^{-+} & A_{gg,e}^{--} \end{bmatrix}\begin{bmatrix} \psi_{g,e}^{+} \\ \psi_{g,e}^{-} \end{bmatrix}+\sum_{g'\neq g}\begin{bmatrix} A_{gg',e}^{++} & A_{gg',e}^{+-} \\ 0 & A_{gg',e}^{--} \end{bmatrix}\begin{bmatrix} \psi_{g',e}^{+} \\ \psi_{g',e}^{-} \end{bmatrix}=\begin{bmatrix} F_{e} & K_{g,e} \\ 0 & \Sigma_{t,g}^{-1} \end{bmatrix}\begin{bmatrix} Q_{g,e}^{+} \\ Q_{g,e}^{-} \end{bmatrix}, \tag{2.21}$$

or more simply

$$A_{gg,e}\psi_{g,e}+\sum_{g'\neq g}A_{gg',e}\psi_{g',e}=B_{g,e}Q_{g,e}. \tag{2.22}$$

We can partition equation 2.22 over energy and define

$$\begin{bmatrix} A_{11,e} & A_{1G,e} \\ A_{G1,e} & A_{GG,e} \end{bmatrix}\begin{bmatrix} \psi_{1,e} \\ \psi_{G,e} \end{bmatrix}=\begin{bmatrix} B_{1,e} & 0 \\ 0 & B_{G,e} \end{bmatrix}\begin{bmatrix} Q_{1,e} \\ Q_{G,e} \end{bmatrix}, \tag{2.23}$$

which can be written compactly as

$$A_{e}\psi_{e}=B_{e}Q_{e}. \tag{2.24}$$

Equation 2.24 is only valid for a single element and we must treat the even-parity flux in a continuous form and the odd-parity flux in a discontinuous form. To do that, we add mapping functions from an assembled vector to the element-wise quantities. For the discontinuous odd-parity vectors the element wise contributions are mapped in a non-overlapping way.

$$\begin{bmatrix} \Xi_{e,+}A_{gg,e}^{++}\Xi_{e,+}^{T} & \Xi_{e,+}A_{gg,e}^{+-}\Xi_{e,-}^{T} \\ \Xi_{e,-}A_{gg,e}^{-+}\Xi_{e,+}^{T} & \Xi_{e,-}A_{gg,e}^{--}\Xi_{e,-}^{T} \end{bmatrix}\begin{bmatrix} \psi_{g}^{+} \\ \psi_{g}^{-} \end{bmatrix}+\sum_{g'\neq g}\begin{bmatrix} \Xi_{e,+}A_{gg',e}^{++}\Xi_{e,+}^{T} & \Xi_{e,+}A_{gg',e}^{+-}\Xi_{e,-}^{T} \\ 0 & \Xi_{e,-}A_{gg',e}^{--}\Xi_{e,-}^{T} \end{bmatrix}\begin{bmatrix} \psi_{g',e}^{+} \\ \psi_{g',e}^{-} \end{bmatrix}$$
$$=\begin{bmatrix} \Xi_{e,+}F_{e} & \Xi_{e,+}K_{g,e}\Xi_{e,-}^{T} \\ 0 & \Xi_{e,-}\Sigma_{t,g}^{-1}\Xi_{e,-}^{T} \end{bmatrix}\begin{bmatrix} Q_{g}^{+} \\ Q_{g}^{-} \end{bmatrix}, \tag{2.25}$$

Summing this equation over all elements in the domain will generate a complete system which we denote compactly as

$$A\Psi=Q, \tag{2.26}$$

The purpose of the SN2ND solver is to obtain time dependent, adjoint, and steady state eigenvalue solutions. In this context, equation 2.26 specifies a fixed source formulation which we can use as a starting point for its wider application needs. As an example, the power method typically used for obtaining the steady state eigenvalue and eigenvector can be written as

$$A\Psi = \frac{1}{k} X\Psi = \frac{1}{k} Q \quad \leftrightarrow \quad \Psi = \frac{1}{k} A^{-1} Q \quad \rightarrow \quad Q^{i+1} = \frac{1}{k^i} X A^{-1} Q^i \tag{2.27}$$

where X represents the fission source operator. In this case k and Q are the fundamental eigenvalue and eigenvector which is all that is desired for most steady state calculations. As seen in equation 2.27, the power method is an iterative technique used to generate the fundamental eigenvalue and eigenvector, where the additional equation

$$k^{i+1} = k^i \frac{\left\| Q^{i+1} \right\|_1}{\left\| Q^i \right\|_1}, \tag{2.28}$$

is used to update the eigenvalue and complete the system.

2.2 SN2ND Transition to a GMRES Based Solution Algorithm

Given that A is large and it is not practical to construct its inverse; an iterative inversion technique is used to approximate the inverse in equation 2.27. In the previous version of SN2ND without parallelism in energy, a Gauss-Seidel (GS) iterative scheme was used to invert A in equation 2.27 which can be written as

$$A\Psi = b \quad \rightarrow \quad (L+D)\Psi^{j+1} = b - U\Psi^j \quad \rightarrow \quad \Psi^{j+1} = (L+D)^{-1}\left[b - U\Psi^j\right]. \tag{2.29}$$

As can be seen, the coefficient matrix is factored into strictly lower triangular L, strictly upper triangular U, and diagonal D components. The inversion of $(L+D)^{-1}$ is the solution of each within-group equation, sequenced with respect to group number, where the up-scattering components, U in equation 2.29, are iteratively lagged. With regard to parallelism in energy, GS is not a scalable algorithm for most reactor calculations of interest because of the physical properties of the scattering (lower triangular dominate scattering). To overcome this limitation in SN2ND, GS is replaced with the Generalized Minimum RESidual (GMRES) algorithm [12, 13] operating on the entire space-angle-energy system. In GMRES, the sequenced solution algorithm of GS is swapped with a series of scalable coefficient matrix-vector applications ($A\Psi^j, A\Psi^{j+1}, A\Psi^{j+2}, \ldots$), a scalable vector orthogonalization, and ideally a scalable preconditioner. <u>Note that a scalable preconditioner remains to be researched and will take significant development time</u>.

Continuing with the GMRES formulation changes, we present the matrix-vector application here because of its complexity. In GMRES, we must apply $Y = AX$ which we will do using an element-wise vector space consistent with equations 2.4 through 2.26. We begin with

$$Y = \begin{bmatrix} A_{11,e} & A_{1G,e} \\ A_{G1,e} & A_{GG,e} \end{bmatrix} X, \tag{2.30}$$

and, mimicking the form of equation 2.25

$$Y = \begin{bmatrix} \Xi_{e,+} A^{++}_{gg,e} \Xi^T_{e,+} & \Xi_{e,+} A^{+-}_{gg,e} \Xi^T_{e,-} \\ \Xi_{e,-} A^{-+}_{gg,e} \Xi^T_{e,+} & \Xi_{e,-} A^{--}_{gg,e} \Xi^T_{e,-} \end{bmatrix} X_g + \sum_{g' \neq g} \begin{bmatrix} \Xi_{e,+} A^{++}_{gg',e} \Xi^T_{e,+} & \Xi_{e,+} A^{+-}_{gg',e} \Xi^T_{e,-} \\ 0 & \Xi_{e,-} A^{--}_{gg',e} \Xi^T_{e,-} \end{bmatrix} X_{g'}. \tag{2.31}$$

The reflected boundary condition modifications are easy to apply given that the starting X vector is scatter-gathered to fill the ghosted part with respect to angle. From there we can obtain the X vector for all visible elements and focus on the within-group form:

$$\begin{bmatrix} Y_{g,e,+} \\ Y_{g,e,-} \end{bmatrix} = \begin{bmatrix} A^{++}_{gg,e} & A^{+-}_{gg,e} \\ A^{-+}_{gg,e} & A^{--}_{gg,e} \end{bmatrix} \begin{bmatrix} X_{g,e,+} \\ X_{g,e,-} \end{bmatrix} + \sum_{g' \neq g} \begin{bmatrix} A^{++}_{gg',e} & A^{+-}_{gg',e} \\ 0 & A^{--}_{gg',e} \end{bmatrix} \begin{bmatrix} X_{g',e,+} \\ X_{g',e,-} \end{bmatrix}. \tag{2.32}$$

Looking at these terms we have to apply

$$A^{++}_{gg',e} = \delta_{gg'} \begin{bmatrix} A_{g,e,1} & 0 \\ 0 & A_{g,e,N} \end{bmatrix} - \begin{bmatrix} W^{+}_{gg',e,1,1} & W^{+}_{gg',e,1,N} \\ W^{+}_{gg',e,N,1} & W^{+}_{gg',e,N,N} \end{bmatrix} \begin{bmatrix} F_e & 0 \\ 0 & F_e \end{bmatrix}. \tag{2.33}$$

$$A^{+-}_{gg',e} = -\begin{bmatrix} K_{g,e,1} & 0 \\ 0 & K_{g,e,N} \end{bmatrix} \begin{bmatrix} W^{-}_{gg',e,1,1} & W^{-}_{gg',e,1,N} \\ W^{-}_{gg',e,N,1} & W^{-}_{gg',e,N,N} \end{bmatrix}. \tag{2.34}$$

$$A^{--}_{gg',e} = \delta_{g,g'} \begin{bmatrix} I & 0 \\ 0 & I \end{bmatrix} - \frac{1}{\Sigma_{t,g}} \begin{bmatrix} W^{-}_{gg,e,1,1} & W^{-}_{gg,e,1,N} \\ W^{-}_{gg,e,N,1} & W^{-}_{gg,e,N,N} \end{bmatrix}. \tag{2.35}$$

$$A^{-+}_{gg',e} = \begin{bmatrix} L_{g,e,1} & 0 \\ 0 & L_{g,e,N} \end{bmatrix}. \tag{2.36}$$

We note that in all of these relationships, the $W^{\pm}_{gg',e,n,n'}$ matrices are needed which require contribution from other groups to the current group, assumed to be owned by a given processor. Since these matrices are collective on the angle-energy communicator, but not on space, we are clear to work only with the element-wise notation shown.

The first step in the process is to apply the collective operations in angle where we will assume that we need the source for all local angles. Starting with the assembled system by direction we have

$$\begin{bmatrix} Y_{g,e,+} \\ Y_{g,e,-} \end{bmatrix} = \begin{bmatrix} A^{++}_{gg,e} & A^{+-}_{gg,e} \\ A^{-+}_{gg,e} & A^{--}_{gg,e} \end{bmatrix} \begin{bmatrix} X_{g,e,+} \\ X_{g,e,-} \end{bmatrix} + \sum_{g' \neq g} \begin{bmatrix} A^{++}_{gg',e} & A^{+-}_{gg',e} \\ 0 & A^{--}_{gg',e} \end{bmatrix} \begin{bmatrix} X_{g',e,+} \\ X_{g',e,-} \end{bmatrix}. \tag{2.37}$$

If we define the matrices

$$W^{++}_{gg',e} = \begin{bmatrix} W^{+}_{gg',e,1,1} & W^{+}_{gg',e,1,N} \\ W^{+}_{gg',e,N,1} & W^{+}_{gg',e,N,N} \end{bmatrix}. \tag{2.38}$$

$$W^{--}_{gg',e} = \begin{bmatrix} W^{-}_{gg',e,1,1} & W^{-}_{gg',e,1,N} \\ W^{-}_{gg',e,N,1} & W^{-}_{gg',e,N,N} \end{bmatrix}. \tag{2.39}$$

Then we can redefine the matrices

$$A^{++}_{gg',e} = \delta_{gg'} \begin{bmatrix} A_{g,e,1} & 0 \\ 0 & A_{g,e,N} \end{bmatrix} - \begin{bmatrix} F_e & 0 \\ 0 & F_e \end{bmatrix} W^{++}_{gg',e} = J^{++}_{gg',e} - F_e W^{++}_{gg',e}. \tag{2.40}$$

$$A^{+-}_{gg',e} = -\begin{bmatrix} K_{g,e,1} & 0 \\ 0 & K_{g,e,N} \end{bmatrix} W^{--}_{gg',e} = -K_{g,e} W^{--}_{gg',e}. \tag{2.41}$$

$$A^{--}_{gg',e} = \delta_{g,g'} \begin{bmatrix} I & 0 \\ 0 & I \end{bmatrix} - \frac{1}{\Sigma_{t,g}} W^{--}_{gg',e} = J^{--}_{gg',e} - \Sigma^{-1}_{t,g} W^{--}_{gg',e}. \tag{2.42}$$

$$A^{-+}_{gg',e} = -\begin{bmatrix} L_{g,e,1} & 0 \\ 0 & L_{g,e,N} \end{bmatrix}. \tag{2.43}$$

The matrix-vector system can now be written as

$$\begin{bmatrix} Y_{g,e,+} \\ Y_{g,e,-} \end{bmatrix} = \begin{bmatrix} J^{++}_{gg',e} - F_e W^{++}_{gg',e} & -K_{g,e} W^{--}_{gg',e} \\ A^{-+}_{gg,e} & J^{--}_{gg',e} - \Sigma^{-1}_{t,g} W^{--}_{gg',e} \end{bmatrix} \begin{bmatrix} X_{g,e,+} \\ X_{g,e,-} \end{bmatrix} + \sum_{g' \neq g} \begin{bmatrix} -F_e W^{++}_{gg',e} & -K_{g,e} W^{--}_{gg',e} \\ 0 & -\Sigma^{-1}_{t,g} W^{--}_{gg',e} \end{bmatrix} \begin{bmatrix} X_{g',e,+} \\ X_{g',e,-} \end{bmatrix}. \tag{2.44}$$

We can rearrange this system by collecting on the $W^{\pm}_{gg',e}$ matrices to define

$$\begin{bmatrix} Y_{g,e,+} \\ Y_{g,e,-} \end{bmatrix} = \begin{bmatrix} J^{++}_{gg',e} & 0 \\ A^{-+}_{gg,e} & J^{--}_{gg',e} \end{bmatrix} \begin{bmatrix} X_{g,e,+} \\ X_{g,e,-} \end{bmatrix} + \sum_{g'} \begin{bmatrix} -F_e W^{++}_{gg',e} & -K_{g,e} W^{--}_{gg',e} \\ 0 & -\Sigma^{-1}_{t,g} W^{--}_{gg',e} \end{bmatrix} \begin{bmatrix} X_{g',e,+} \\ X_{g',e,-} \end{bmatrix}. \tag{2.45}$$

We note that the first term in this system has no connection in angle while the second requires the collection on the angular system (conversion to/from spherical harmonics). We can further modify the second term to define

$$\begin{bmatrix} Y_{g,e,+} \\ Y_{g,e,-} \end{bmatrix} = \begin{bmatrix} J^{++}_{gg',e} & 0 \\ A^{-+}_{gg,e} & J^{--}_{gg',e} \end{bmatrix} \begin{bmatrix} X_{g,e,+} \\ X_{g,e,-} \end{bmatrix} - \sum_{g'} \begin{bmatrix} F_e & K_{g,e} \\ 0 & \Sigma^{-1}_{t,g} \end{bmatrix} \begin{bmatrix} W^{++}_{gg',e} & 0 \\ 0 & W^{--}_{gg',e} \end{bmatrix} \begin{bmatrix} X_{g',e,+} \\ X_{g',e,-} \end{bmatrix}. \tag{2.46}$$

From here we can define the intermediate vector

$$\begin{bmatrix} Z_{g,e,+} \\ Z_{g,e,-} \end{bmatrix} = \sum_{g'} \begin{bmatrix} W^{++}_{gg',e} & 0 \\ 0 & W^{--}_{gg',e} \end{bmatrix} \begin{bmatrix} X_{g',e,+} \\ X_{g',e,-} \end{bmatrix}, \tag{2.47}$$

which gives the system

$$\begin{bmatrix} Y_{g,e,+} \\ Y_{g,e,-} \end{bmatrix} = \begin{bmatrix} J^{++}_{gg',e} & 0 \\ A^{-+}_{gg,e} & J^{--}_{gg',e} \end{bmatrix} \begin{bmatrix} X_{g,e,+} \\ X_{g,e,-} \end{bmatrix} - \begin{bmatrix} F_e & K_{g,e} \\ 0 & \Sigma^{-1}_{t,g} \end{bmatrix} \begin{bmatrix} Z_{g,e,+} \\ Z_{g,e,-} \end{bmatrix}. \tag{2.48}$$

Now none of the remaining matrices in equation 2.48 requires communication in angle or energy and we have collected the entire communication requirements in defining the intermediate vector $Z_{g,e}$. In short, the matrices above are block diagonal with respect to angle and energy. With parallelism in energy there is no way to eliminate the need for the $Z_{g,e}$ vector storage. So while a GS algorithm requires a single vector with duplicated storage on the within-group equation, a GMRES algorithm will require 3 vectors of the full energy-angle and discontinuous space size assigned to the local process. Of course the GMRES requirements itself will dwarf this (30 back vectors is 10 times this storage). Note that the remaining steps after obtaining the element $Y_{g,e}$ vector are relatively straightforward although reflective boundary conditions do require additional communication on the angular communicator to merge and zero the appropriate solution moments.

2.3 SN2ND Spatial Multigrid Preconditioning Scheme

The most important development area identified for SN2ND was the need for a spatial multigrid preconditioning concept. Fundamentally, the desire to solve heterogeneous geometries translates to hundreds of millions of spatial degrees of freedom (mesh vertices). The existing SOR preconditioned CG algorithm provided by PETSc is very good for 0.2 to 1.5 million vertex problems but its performance drops off rapidly beyond that. Further, since heterogeneous geometries are utilizing mesh sizes much smaller than those appearing in the homogenized calculations associated with the conventional experience (0.2 to 1.5 million), SOR is simply inadvisable. While we can switch the preconditioner to an algebraic multigrid

option, also available through PETSc, the memory requirements are increased by a factor of 2 or more which hurts performance and problem size substantially (i.e. 70 group calculations will not be solvable on modern supercomputing machines with the old SN2ND solver). After doing the preliminary research on spatial multigrid we have chosen a very specific approach for use with the GMRES algorithm and parallelization in energy.

Introducing a generic hierarchical spatial multigrid concept is very complicated and required new data structures and algorithms specific to SN2ND (i.e. not usable by MOCFE). To understand how multi-grid is implemented, we constrain our focus to the within-group even-parity system defined as

$$A\tilde{\psi}^{+} = b^{+} . \tag{2.49}$$

We can define a preconditioner for equation 2.49 as

$$M_g^{-1} A_g \tilde{\psi}_g^{+} = M_g^{-1} b_g^{+} \quad \rightarrow \quad Y = M_g^{-1}\left\{ b_g^{+} - A_g \tilde{\psi}_g^{+} \right\} = M_g^{-1} X = 0 \quad \rightarrow \quad M_g Y = X . \tag{2.50}$$

In equation 2.50, we always define a preconditioner M_g that is representative of the coefficient matrix in equation 2.49, but typically much simpler. The matrix M_g is rarely directly invertible and thus some numerical inversion technique such as GS or SOR is used. In SN2ND, a CG algorithm is used over the entire space-angle system for equation 2.49 and the coupling in angle is neglected in the preconditioner M_g [2] such that each angular subsystem $M_{g,n}$ can be solved simultaneously. The matrix $M_{g,n}$ is symmetric positive definite and we again utilize a CG algorithm to perform the necessary inversion appearing in equation 2.50. With such a scheme, we can write

$$M_{g,n} Y_n = X_n \;\; \& \;\; \left(M_{g,n}^{'} \right)^{-1} \left\{ X_n - M_{g,n} Y_n \right\} = 0 \quad \rightarrow \quad M_{g,n}^{'} Y_n^{'} = X_n^{'} , \tag{2.51}$$

where $M_{g,n}^{'}$ is a preconditioner for the CG iterative scheme involving $M_{g,n}$. One can easily see how this process can continue in a hierarchical fashion where each new CG level will generate a simpler preconditioner.

This is fundamentally the concept behind developing a multi-grid preconditioner where the spatial "grid" becomes progressively coarser and thus cheaper from a numerical inversion point of view. The reason this approach is scalable and efficient is that the coefficient matrix application at each level is scalable at each preconditioner level of $M_{g,n}$. In our particular case, because the $M_{g,n}$ were made independent in angle, the approach also shows improvements in communication costs.

2.4 Development of a Multi-grid Preconditioner

The existing SN2ND solver utilizes a parallel CG algorithm in PETSc to invert $M_{g,n}$ with a parallel SOR preconditioner $M_{g,n}^{'}$. In FY2009 a *p*-multigrid preconditioner was attempted as a quick fix to circumvent a memory related problem on BlueGene/P [20]. This introduces a single level to the scheme outlined by equations 2.50 and 2.51 written as

$$\begin{aligned} M_{g,n}Y_n &= X_n \;\;\&\;\; Y_n^{'} = \left(M_{g,n}^{'}\right)^{-1}\left\{X_n - M_{g,n}Y_n\right\} = \left(M_{g,n}^{'}\right)^{-1} X_n^{'} \\ M_{g,n}^{'}Y_n^{'} &= X_n^{'} \;\;\&\;\; Y_n^{''} = \left(M_{g,n}^{''}\right)^{-1}\left\{X_n^{'} - M_{g,n}^{'}Y_n^{'}\right\} = \left(M_{g,n}^{''}\right)^{-1} X_n^{''} \end{aligned} . \tag{2.52}$$

The application of $M_{g,n}$ was switched from an assembled and stored matrix operation performed by PETSc to a matrix-free operation carried out in a subroutine of SN2ND. Given a mesh with quadratic finite elements, the preconditioner $M_{g,n}^{'}$ would have the same mesh but utilize linear finite element trial functions. In the *p*-multigrid version the lower order system $M_{g,n}^{'}$ is assembled and given to PETSc so that it can apply CG with a parallel SOR preconditioner at the $M_{g,n}^{''}$ level.

The *p*-multigrid preconditioning scheme outlined above failed miserably. The primary issue was that the linear mesh did not span the vector space of the originating quadratic (or higher order) mesh and thus the spatial multigrid concept required a smoothing step. Because of the incompatible data structures of SN2ND, all that could be implemented in a reasonable amount of time was an inefficient Jacobi smoothing step. While this may seem a poor choice from both an implementation and theory point of view, it was done as a quick fix to circumvent the memory related issues on BlueGene/P. Overall, this turned out to be an instructive learning experience that proved reliance upon specific examples from the literature are not necessarily appropriate because the typical case study focuses on structured grids with fixed material properties that are not terribly heterogeneous such as that observed for a fuel assembly in a nuclear reactor or a explicitly represented ZPR drawer.

Because the literature is not clear on what preconditioner will work best, the two primary authors of the SN2ND solver decided it was best to consult experts on multigrid methodologies [10] rather than attempt another implementation in SN2ND that duplicated the experiences with the first multigrid implementation. Those discussions also considered the impact that parallelization in energy would have and the ongoing issues associated with memory usage. While algebraic multigrid [11] is the optimal strategy for symmetric positive definite systems, the increased memory load negates it on current supercomputers and those expected to come for neutronics calculations. The outcome of those discussions was to incorporate the spatial multigrid preconditioner simultaneously with the GMRES solver on the multigroup system. Starting with the multigroup system as

$$A\Psi = Q \quad \rightarrow \quad Au = b \quad \rightarrow \quad A_0 y_0 + r_0 = x_0 , \tag{2.53}$$

where u is the exact solution, x is the source on the originating grid, y is an approximate answer on the originating grid and r is the associated residual. Using this notation we can define a single step spatial multigrid approach as

$$\begin{aligned}
&y_0 = smooth\left(A_0^{-1}x_0\right)\\
&r_0 = x_0 - A_0 y_0\\
&\quad x_1 = R_{0\to 1} r_0\\
&\quad y_1 = solve\left(A_1^{-1}x_1, tolerance\right)\\
&y_0 = y_0 + P_{1\to 0} y_1\\
&y_0 = smooth\left(A_0^{-1}x_0\right)
\end{aligned}, \tag{2.54}$$

and a two step multigrid approach as

$$\begin{aligned}
&y_0 = smooth\left(A_0^{-1}x_0\right)\\
&r_0 = x_0 - A_0 y_0\\
&\quad x_1 = R_{0\to 1} r_0\\
&\quad y_1 = smooth\left(A_1^{-1}x_1\right)\\
&\quad r_1 = x_1 - A_1 y_1\\
&\qquad x_2 = R_{1\to 2} r_1\\
&\qquad y_2 = solve\left(A_2^{-1}x_2, tolerance\right)\\
&\quad y_1 = y_1 + P_{2\to 1} y_2\\
&\quad y_1 = smooth\left(A_1^{-1}x_1\right)\\
&y_0 = y_0 + P_{1\to 0} y_1\\
&y_0 = smooth\left(A_0^{-1}x_0\right)
\end{aligned}. \tag{2.55}$$

In both equations 2.54 and 2.55, the smooth operations are in fact a high error solve operations involving just a few iterations (3-5) and the matrices $R_{0\to 1}$ and $P_{1\to 0}$ are restriction and prolongation matrices respectively. For SN2ND, we have implemented the two step spatial multigrid scheme in equation 2.55 as part of the multigroup preconditioning step and thus define the preconditioner algorithm

$$\begin{aligned}
&x_1 = R_{0\to 1} x_1\\
&Block\,GS \quad \begin{cases} b_{1,g} = \sum_{g'} A_{1,g'\to g} x_{1,g'} \\ y_{1,g} = solve\left(A_{1,gg}^{-1} b_{1,g}, tolerance\right) \end{cases}\\
&y_0 = P_{1\to 0} y_1
\end{aligned}. \tag{2.56}$$

The preconditioner for the solve step in equation 2.56 is then defined identically to equations 2.54 or 2.55 depending upon the number of multigrid steps involved.

It is important to note that there is no smoothing operation in equation 2.56 although they are quite prevalent in equations 2.54 and 2.55. This is primarily because of the particular spatial multigrid step used and graphically depicted in Figure 2.1.

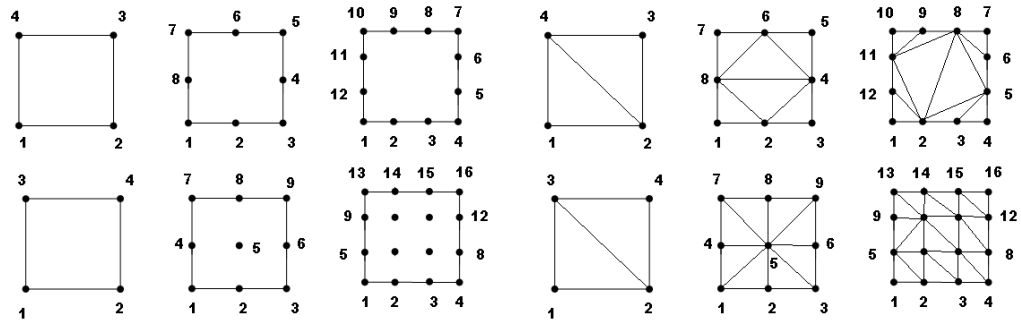

Figure 2.1 Serendipity (upper six) and Lagrangian (lower six) Quadrilaterals (left six) and their Tessellated Counterparts (right six)

From Figure 2.1, it should be clear that the number of spatial degrees of freedom for the assembled system is identical. For the odd-parity discontinuous system, we have an interpolative scheme. In short, this spatial multigrid step, which we term a linear tessellation or *LT*-multigrid since it does not match conventional *p*- or *h*- concepts, spans the originating higher order space in both the continuous and discontinuous form and thus does not require a smoothing step. For the additional multigrid steps we have only considered a single step depicted in Figure 2.2.

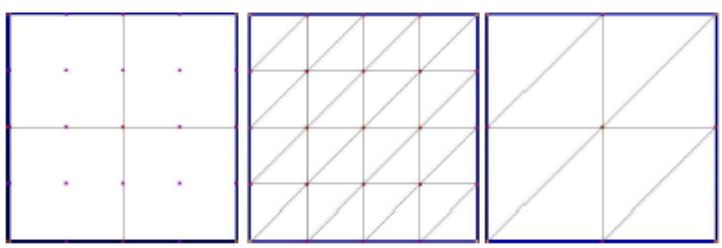

Figure 2.2 Current Multigrid Steps Available in the new SN2ND Solver

In Figure 2.2, the left most picture is the original mesh consisting of four Lagrangian Quadrilaterals, the center picture is a tessellated triangular mesh of the left hand mesh (note that the tessellation is different than that of Figure 2.1), and the right hand picture is the tessellation of the originating mesh truncated to a linear order. For curvilinear geometries, the volume of each originating element in Figure 2.2 is preserved when applying the tessellation and the truncation to a linearly tessellated system. Beyond this point, it is not clear whether algebraic multigrid or additional spatial multigrid is wise and thus additional research is needed. Fundamentally, SN2ND is hardwired to assume that the linear tessellation step occurs as part of the multigroup preconditioning step. Beyond that, it is a rather easy process to modify the existing algorithm to define additional steps.

2.5 Implementation Concerns about Spatial Multigrid

It is important to note that even though the originating even-parity system outlined by equation 2.49 is symmetric positive definite, the Flexible GMRES (FGMRES) algorithm [13] is used on the smoothing operations and each level of the multigrid preconditioning in equation 2.55 except the last. This is necessary because the prolongation and restriction operators make the preconditioner different from the coefficient matrix (i.e. not symmetric

positive definite) and the fact that on each level we are not exactly solving the lower steps. In such a case, the lack of convergence in the preconditioner leads to noise which can cause GMRES and CG to fail to converge.

The preceding multigrid scheme was cooked up only considering the continuous even-parity system. After doing considerable research on how h-coarsening was applied for first order discrete ordinates methods, concern arose with respect to how using the linear tessellation would impact the odd-parity system which is similarly treated discontinuously. Of course, a first order discrete ordinates methods must concern itself with transmission of the current (i.e. the current representation must also be included in the projection/restriction) which is not the case with the SN2ND solver. A simple example to display the concern is shown in Figure 2.3 where the tessellation is observed to introduce a new line of discontinuity.

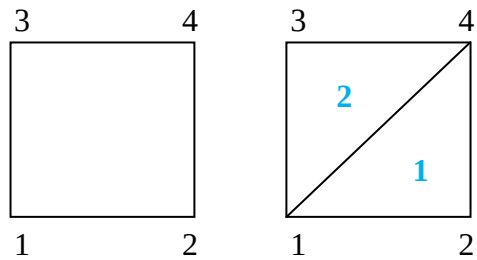

Figure 2.3 Quadrilateral (left) and Triangularly Tessellated Quadrilateral (right)

The idea behind the tessellation is that the even-parity continuous vector space is identical between these two elements (i.e. four degrees of freedom per direction per group), but the odd-parity vector space is not. In Figure 2.3, the discontinuous odd-parity flux will have four degrees of freedom for a linear quadrilateral (left) and six degrees of freedom for two linear triangles, respectively. When there is no anisotropic scattering, the odd-parity flux within each node can be written as:

$$\psi_g^-(\vec{r},\hat{\Omega}) = -\frac{1}{\Sigma_{t,g}(\vec{r})}\hat{\Omega}\cdot\vec{\nabla}\psi_g^+(\vec{r},\hat{\Omega}) + \frac{1}{\Sigma_{t,g}(\vec{r})}W_g^-(\vec{r},\hat{\Omega}) + \frac{1}{\Sigma_{t,g}(\vec{r})}S_g^-(\vec{r},\hat{\Omega}). \tag{2.57}$$

This can be rewritten in a discrete form for the finite element system above as

$$\tilde{\psi}_{g,n}^- = -\frac{1}{\Sigma_{t,g}}\sum_k \hat{\Omega}_n^k F^{-1}U_k\tilde{\psi}_{g,n}^+ + \frac{1}{\Sigma_{t,g}}F^{-1}\tilde{W}_{g,n}^- + \frac{1}{\Sigma_{t,g}}F^{-1}\tilde{S}_{g,n}^-. \tag{2.58}$$

For the two-dimensional geometries in Figure 2.3, we only need to study the $F^{-1}U_1$ matrix component to understand the fundamental problem with introducing a discontinuity in the solution. Equation 2.59 gives the evaluated matrices for an elongated quadrilateral.

$$F^{-1}U_{quad,1} = \begin{bmatrix} -3\tfrac{1}{3} & 0 & 3\tfrac{1}{3} & 0 \\ 0 & -3\tfrac{1}{3} & 0 & 3\tfrac{1}{3} \\ -3\tfrac{1}{3} & 0 & 3\tfrac{1}{3} & 0 \\ 0 & -3\tfrac{1}{3} & 0 & 3\tfrac{1}{3} \end{bmatrix} \qquad \begin{aligned} F^{-1}U_{tri=1,1} &= \begin{bmatrix} 0 & -3\tfrac{1}{3} & 3\tfrac{1}{3} \\ 0 & -3\tfrac{1}{3} & 3\tfrac{1}{3} \\ 0 & -3\tfrac{1}{3} & 3\tfrac{1}{3} \end{bmatrix} \\ F^{-1}U_{tri=2,1} &= \begin{bmatrix} -3\tfrac{1}{3} & 0 & 3\tfrac{1}{3} \\ -3\tfrac{1}{3} & 0 & 3\tfrac{1}{3} \\ -3\tfrac{1}{3} & 0 & 3\tfrac{1}{3} \end{bmatrix} \end{aligned} \tag{2.59}$$

From equation 2.59 one can see that the values of the coefficient matrices are similar and multiplication by a random even-parity continuous vector is found to yield

$$F^{-1}U_{quad,1}\begin{bmatrix} 7 \\ 3 \\ 2 \\ 8 \end{bmatrix} = \begin{bmatrix} -16\tfrac{2}{3} \\ 16\tfrac{2}{3} \\ -16\tfrac{2}{3} \\ 16\tfrac{2}{3} \end{bmatrix} \qquad \begin{aligned} F^{-1}U_{tri=1,1}\begin{bmatrix} 7 \\ 3 \\ 8 \end{bmatrix} &= \begin{bmatrix} 16\tfrac{2}{3} \\ 16\tfrac{2}{3} \\ 16\tfrac{2}{3} \end{bmatrix} \\ F^{-1}U_{tri=2,1}\begin{bmatrix} 7 \\ 8 \\ 2 \end{bmatrix} &= \begin{bmatrix} -16\tfrac{2}{3} \\ -16\tfrac{2}{3} \\ -16\tfrac{2}{3} \end{bmatrix} \end{aligned}. \tag{2.60}$$

Similar to equation 2.59, the values generated in equation 2.60 by both approaches are also very similar. Application of the injection based prolongation matrix required to project from the tessellated odd-parity to the original system yields

$$\begin{bmatrix} 0.5 & 0 & 0 \\ 0 & 1 & 0 \\ 0 & 0 & 0 \\ 0 & 0 & 0.5 \end{bmatrix} F^{-1}U_{tri=1,1}\begin{bmatrix} 7 \\ 3 \\ 8 \end{bmatrix} + \begin{bmatrix} 0.5 & 0 & 0 \\ 0 & 0.5 & 0 \\ 0 & 0 & 1 \\ 0 & 0 & 0 \end{bmatrix} F^{-1}U_{tri=2,1}\begin{bmatrix} 7 \\ 8 \\ 2 \end{bmatrix} = \begin{bmatrix} 0 \\ 8\tfrac{1}{3} \\ -16\tfrac{2}{3} \\ 8\tfrac{1}{3} \end{bmatrix} \neq \begin{bmatrix} -16\tfrac{2}{3} \\ 16\tfrac{2}{3} \\ -16\tfrac{2}{3} \\ 16\tfrac{2}{3} \end{bmatrix}. \tag{2.61}$$

From equation 2.61, the injection based prolongation does not yield a solution which would be consistent with the originating quadrilateral and thus there is some obvious concern with regard to whether this will cause divergence or slow convergence of the Krylov solver. In the problems tested thus far, which do have steep gradients, divergence did not occur which is likely because the result is still conservative over each element (i.e. the volume integral yields the same total), but it is not clear as to its impact on performance at this time.

3 SN2ND Validation Work

In this section we focus on the work that was completed using the SN2ND solver in FY2011. A majority of that work was focused on validation work related to ZPR experiments, but additional time was spent doing comparisons on MONJU and attempting several heterogeneous reactor calculations. While the sub-group methodology was researched in FY2011, SN2ND is not presently capable of using it and thus it cannot performing thermal reactor calculations at this time. All of this work was completed with the solver built in 2008 and optimized for routine use in 2009.

3.1 Homogenized Drawer Modeling of ZPR-6 Assembly 7 Experiment

In FY2010, significant time was spent setting up the ZPR-6 Assembly 7 benchmark [15-18] using the BuildZPRmodel [2] to reduce input errors. The intent of that work was to define

a clear procedure for validating the heterogeneous modeling capability available with SN2ND+MC^2-3 using ZPR benchmarks. The goal was to select benchmarks and loadings from several ZPR experiments and compare the eigenvalue and flux solution the latter of which would be done using foil measurements taken during the experiments. In FY2011, the drawer homogenized models were created for loadings 104, 106, 120, and 132 of ZPR-6/7 along with heterogeneous models of ZPR-6/7 loading 104. Figure 3.1 shows the typical drawer homogenized model for loading 106 along with flux solutions obtained using SN2ND, all created using the VISIT visualization tool [21].

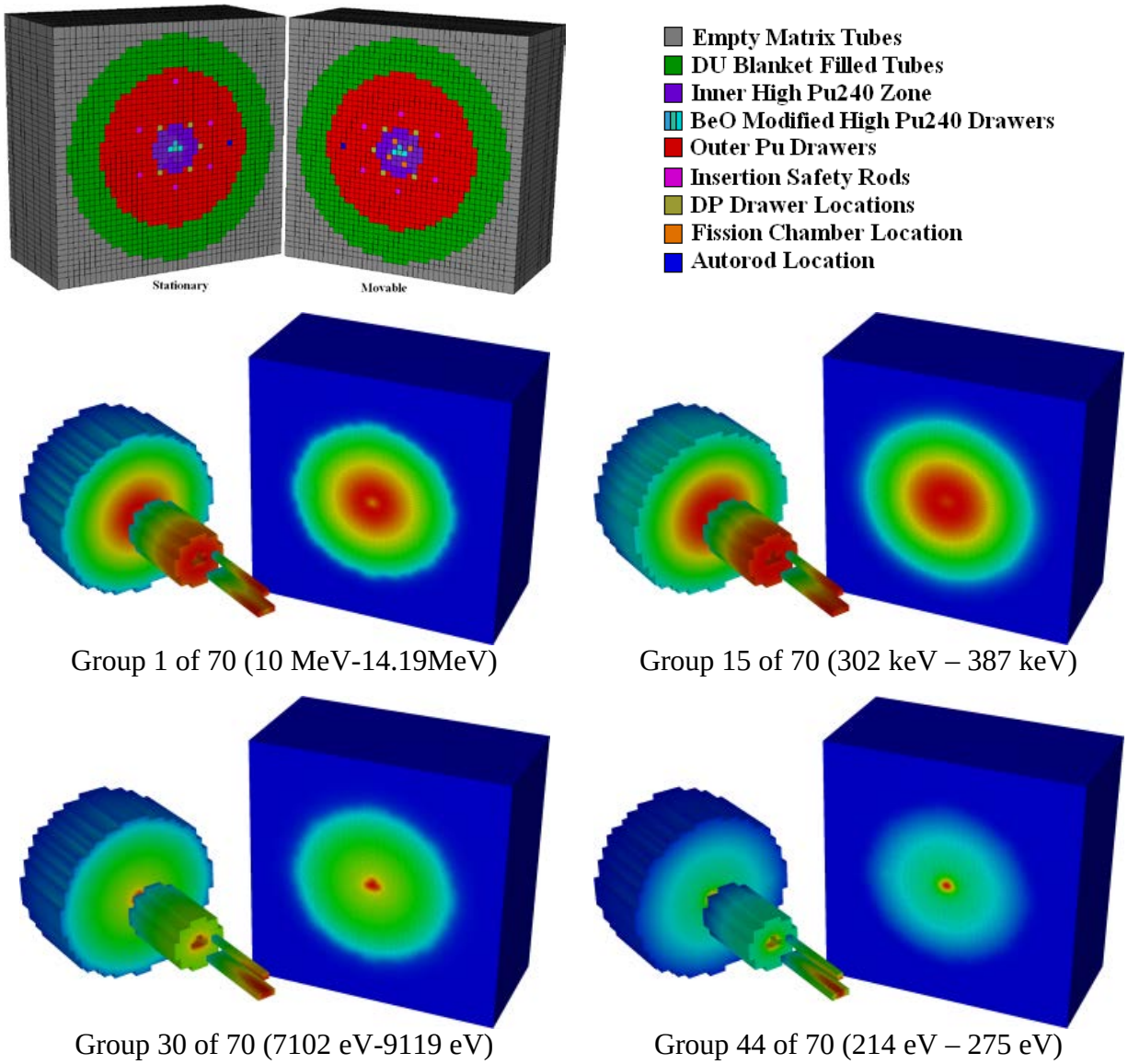

Figure 3.1. ZPR-6/7 Geometry and Selected Flux Plots for Loading 106

For each picture in Figure 3.1, the right hand side of the picture displays the face of the movable matrix while the left hand picture shows the flux solution for the active core portion of the stationary side (everything inside of the blankets). For the stationary side, we separated the high Pu-240 zone to display the axial flux solution along with the central BeO modified

drawers so the axial flux variation can be observed. As can be seen, there is a noticeable thermalization of the flux near the BeO loaded drawers.

Table 3.1 summarizes the calculated SN2ND eigenvalue results for loadings 104, 106, 120, and 132 as compared to MCNP as-built calculations (i.e., every plate, drawer, matrix tube, etc. were modeled explicitly) and the experimentally measured values. As can be seen, the deterministic SN2ND results are generally higher than the MCNP calculations for all but loading 132. However, it is noted that the MCNP solutions generally underestimate the core reactivity compared to the measurements while the SN2ND solutions overestimate them. For all the four core loadings analyzed, the SN2ND solver predicted the core reactivity within 1σ of the estimated experimental uncertainty (~80 pcm) [17, 18]. These results are comparable to the accuracy of MCNP solutions; the SN2ND solutions deviated from the measured values by 75, 43, 28 and -24 pcm for the Loadings 104, 106, 120, and 132, respectively, while the corresponding deviations of MCNP solutions were -56, -42, -132, and 0 pcm.

Table 3.1. ZPR6-7 Loadings 104, 106, 120, and 132 Measured and Calculated Eigenvalues

Loading	UNIC	MCNP	Experimental†
104	1.00147	1.00016 ± 0.00007	1.00072 ± 0.00002
106	1.00134	1.00049 ± 0.00007	1.00091 ± 0.00003
120	1.00127	0.99967 ± 0.00007	1.00099 ± 0.00003
132	1.00016	1.00040 ± 0.00007	1.00040 ± 0.00002

† Measurement uncertainty only, excluding composition and geometry uncertainties

The layout of the foils is given in Figure 3.2. As can be seen, the foils were placed in column 23 below the central position, (i.e., in rows 24–45), and were irradiated in order to measure radial traverses of specific reaction rates. Four types of foils (designated as E, D, p, P) were used to measure relative reaction rates of Enriched Uranium fission (EU f) using E-type foils; Depleted Uranium capture (DU c) and fission (DU f) using D-type foils, and ^{239}Pu fission (Pu49 f) using p- and P-type foils. These foils were placed in 2-inch (5.08 cm) square packets. Each packet consisted of the four foil types sandwiched between a 1-mil (0.00254 cm) aluminum square and a 1-mil stainless steel square on both sides. The packets were placed in the fronts of the drawers of the stationary half between the Fe_2O_3 plate and the fuel plate on the left side of the drawer as one faces the front of the drawer from a position between the halves [17, 18]. Figure 3.2 shows the positions of the foils within the packets and the positions of the packets in the core for the foil irradiations.

Foil percent reaction rate errors ((C/E-1)%) are summarized in Table 3.2. In this table, the Y position corresponds to the center of each foil measured from the center of the first matrix location loaded with foils. In addition, as reported in references 6 and 7, the measured experimental values were arbitrarily normalized to the foil measurements at 66.33 cm so that percent reaction rate errors at this location are identically zero. It can be seen that the results for loadings 104 and 120 are generally acceptable. Most of the errors are within 1σ of the experimental uncertainties with few exceptions: EU(f) at the first few foil positions for loading 104; Pu49(f) in the first few foil positions in both loadings 104 and 120, and Pu49(f) at position Y=10.07 cm in loading 120. More importantly, the results for the homogeneous loadings 106 and 132 exhibit large errors in the calculated DU(c) (certainly more than 3σ of

the experimental uncertainty) for foils inside the first 10 cm, i.e., near foil positions closest to the core central position. (Recall that in these two loadings a BeO ring was inserted to surround the core central location, and in these homogeneous models, the BeO ring was homogenized with the central position's material, i.e., sodium in loading 106 and B_4C in loading 132.) It is also seen that in both of these loadings, large errors are observed for both EU(f) and Pu49(f) in the first and, to a lesser extent, the second foil positions.

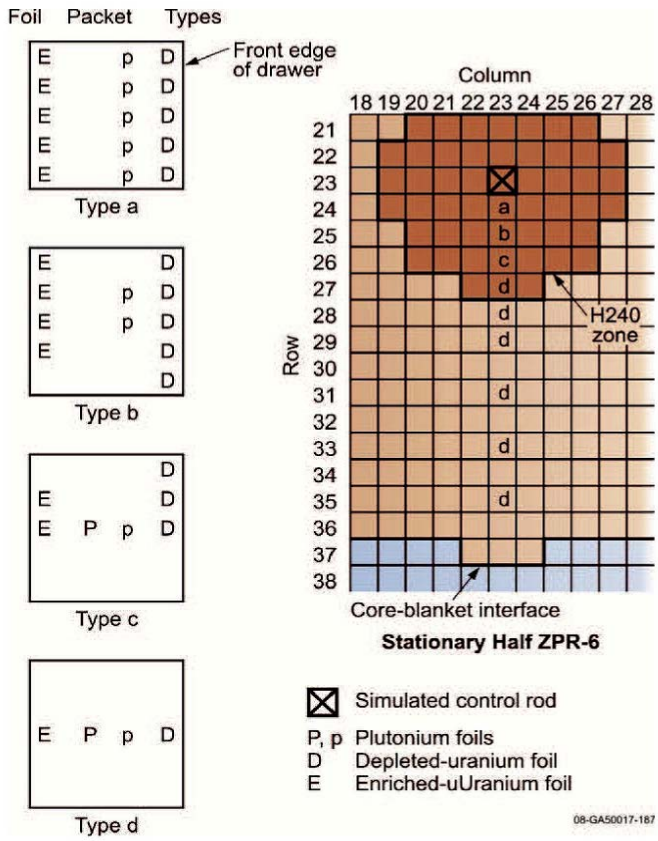

Figure 3.2. ZPR-6/7 Description of Foil Types and Locations

After setting up several calculations using different MC^2-3 models combined with mixed homogeneous-heterogeneous models in SN2ND, we concluded that the primary reason for the errors in the solutions of loadings 106 and 132 was a flaw in the cross section generation approach taken. To properly account for the localized effect of BeO, a two-dimensional MC^2-3 model of the extended central region geometry is necessary which cannot be captured with a one-dimensional model since the BeO plate arrangement is perpendicular to the fuel-drawer plate loading. Since that capability was not available during this work, an MCNP [22] model of the central drawers containing BeO plates was built with the first fuel drawer represented explicitly by its one-dimensional MC^2-3 model equivalent.

Table 3.2. C/E Values in % Error for Normalized Foil Reaction Rates

Foil location (cm)	Loading 104				Loading 106			
	EU f	DU c	DU f	Pu49 f	EU f	DU c	DU f	Pu49 f
3.53	2.60	-0.82	1.25	2.92	-4.83	-16.77	1.69	-5.50
4.55	2.62	0.58	-0.18	3.39	-2.70	-11.05	-1.09	-2.71
5.56	2.73	1.65	-0.34	3.03	-1.29	-6.53	-0.98	-1.01
6.58	2.84	1.79	0.42	3.01	-0.42	-4.64	-0.68	-0.01
7.60	2.61	0.48	1.33	2.40	-0.94	-4.61	0.23	-0.77
9.06	2.29	0.53	2.01		-0.02	-2.55	1.31	
10.07	2.37	1.45	0.80	2.41	0.08	-2.92	0.12	1.07
11.09	2.36	1.89	0.29	2.09	0.59	-0.96	0.01	0.84
12.10	2.05	1.47	0.89		0.30	-1.11	0.19	
13.12		0.59	2.20			-1.30	1.46	
14.58		-1.19	2.54			-1.59	1.93	
15.60	1.43	0.91	1.16		0.11	-0.59	0.42	
16.61	1.67	1.39	0.65	1.64	0.41	0.14	-0.05	1.09
22.14	2.01	1.90	0.79	2.32	0.52	0.87	0.60	1.56
27.66	2.06	0.75	2.28	2.17	1.29	0.33	1.79	2.07
33.19	2.09	0.40	1.88	2.14	1.75	1.22	1.62	1.74
44.24	1.66	-0.94	1.72	1.70	0.87	-0.42	0.92	1.60
55.28	1.88	0.67	1.03	1.01	1.26	1.01	0.40	1.39
66.33	0.00	0.00	0.00	0.00	0.00	0.00	0.00	0.00
Foil location (cm)	Loading 120				Loading 132			
	EU f	DU c	DU f	Pu49 f	EU f	DU c	DU f	Pu49 f
3.53	0.25	0.39	1.18	2.64	-6.35	-13.16	1.84	-4.83
4.55	1.53	2.19	0.20	3.05	-3.81	-8.44	-0.53	-2.13
5.56	1.54	2.29	-0.05	2.91	-1.69	-4.50	-1.09	-1.01
6.58	1.85	1.85	0.11	2.23	-1.10	-3.37	-0.16	-0.79
7.60	1.81	1.27	1.86	2.79	-0.82	-3.68	0.86	-0.46
9.06	1.54	1.20	1.95		-0.53	-2.23	1.12	
10.07	2.13	1.34	0.80	4.96	-0.07	-1.53	-0.07	0.87
11.09	2.00	2.43	0.69	2.69	0.40	-0.91	0.53	0.15
12.10	1.90	1.37	0.77		0.65	0.03	0.73	
13.12		1.34	2.49			-1.22	1.30	
14.58		1.21	2.87			-1.27	2.58	
15.60	1.57	0.85	1.43		0.33	-0.82	1.57	
16.61	1.42	1.57	1.28	2.63	0.37	-0.41	0.73	2.29
22.14	1.82	1.02	0.97	3.04	0.53	0.49	0.74	1.43
27.66	2.01	1.89	2.75	3.10	1.30	0.16	2.24	2.05
33.19	1.80	0.24	2.27	2.28	0.99	0.25	2.12	1.82
44.24	1.58	-0.49	1.47	2.14	0.86	0.55	1.86	1.75
55.28	0.98	0.66	1.39	1.84	1.32	0.98	1.36	1.73
66.33	0.00	0.00	0.00	0.00	0.00	0.00	0.00	0.00

The Monte Carlo geometry was surrounded by a layer of approximately two-drawers-length homogenized fuel composition in the X and Y directions and a reflective boundary condition was imposed on its outer boundaries. The length in the Z direction was manually set to achieve a critical MCNP eigenvalue; thereby simulating a critical spectrum over the heterogeneous fuel drawer. Seventy-group homogenized cross sections for ^{238}U capture and ^{235}U fission were tallied over five different Y-direction sections of the heterogeneous fuel drawer corresponding to the first five foil locations and combined with the SN2ND flux solutions using a MC^2-3 model to produce the results in Table 3.3.

Table 3.3. Comparison of C/E Values (% Error) for Normalized Foil Reaction Rates Determined with Cross Sections from One-Dimensional MC^2-3 and Two-Dimensional MCNP Calculations

Foil location (cm)	Loading 106				Loading 132			
	EU f		DU c		EU f		DU c	
	MC^2-3	MCNP	MC^2-3	MCNP	MC^2-3	MCNP	MC^2-3	MCNP
3.53	-4.83	3.90	-16.77	-2.11	-6.35	3.38	-13.16	1.42
4.55	-2.70	3.67	-11.05	-2.79	-3.81	2.86	-8.44	-0.06
5.56	-1.29	3.81	-6.53	0.02	-1.69	3.21	-4.50	1.84
6.58	-0.42	3.62	-4.64	0.68	-1.10	2.76	-3.37	1.76
7.60	-0.94	2.21	-4.61	-0.24	-0.82	2.21	-3.68	0.54

Table 3.3 compares the C/E values of the EU fission and DU capture reaction rates determined with the cross sections obtained from one-dimensional MC^2-3 and two-dimensional MCNP calculations for the first five foils from the core center. It should be noted that the MCNP cross sections generated for the loading 106 configuration were used for both the loadings 106 and 132. It can be seen that using the foil cross sections obtained from the MCNP calculation, the C/E values for DU capture reactions are improved noticeably for both loadings 106 and 132 even though the central drawer is very different for the two loadings.

3.2 Partially Heterogeneous Modeling of ZPR-6 Assembly 7 Experiment

In addition to the homogeneous modeling cases above, the NEAMS program also needs validation work on the heterogeneous modeling capability. Full core heterogeneous SN2ND calculations like that attempted in FY2009 for ZPR-6/6A are beyond the existing supercomputer capabilities. However, part of the FY2011 work is focused on comparing the change in the solution accuracy as the drawer-homogenization model is replaced with a heterogeneous plate-by-plate model. To study this impact, four partially heterogeneous models of ZPR6-7 loading 104 were created as shown in Figure 3.3, in addition to the base homogeneous model. The intent is to compare the criticality and foil reaction rates with the experimentally measured quantities for each of these models. Plate-by-plate cross sections were generated using MC^2-3. Figure 3.4 shows a close up view of the mesh used in model 1.

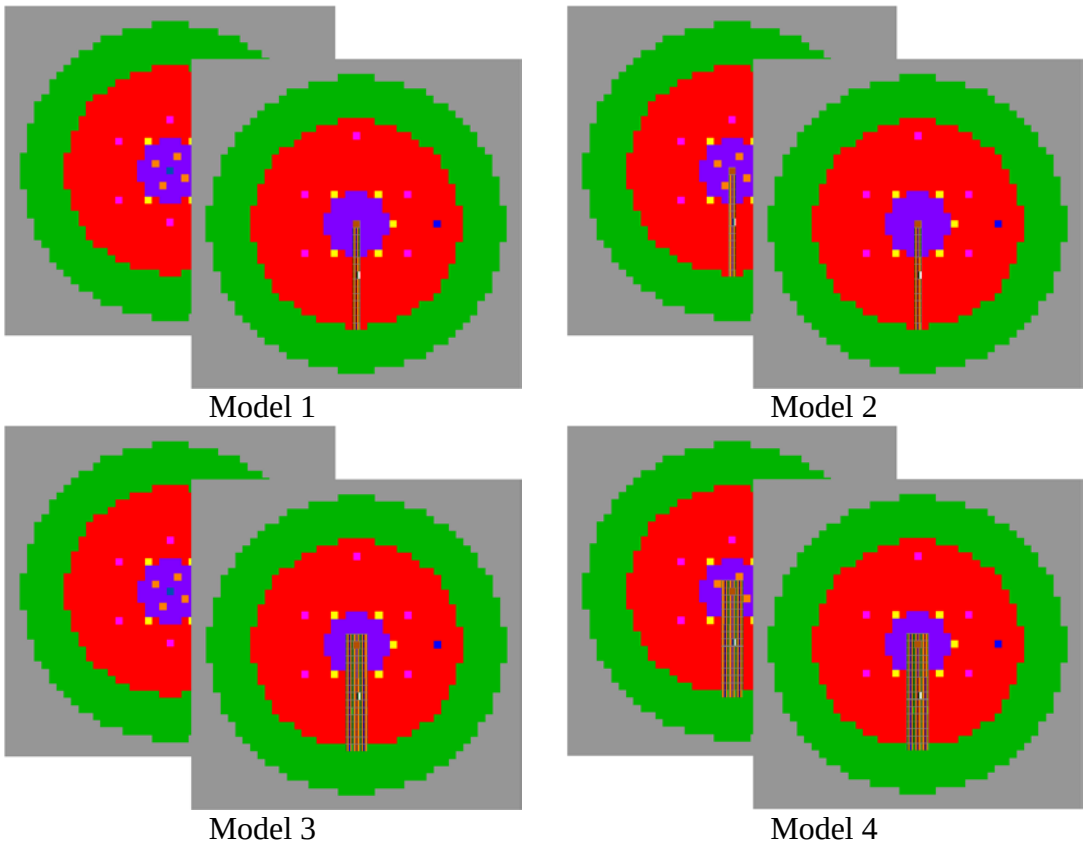

Figure 3.3. Depiction of the Spatial Heterogeneity in the Stationary Matrix Half (Front Picture in Each Model) and Movable Matrix Half (Back Picture in Each Model).

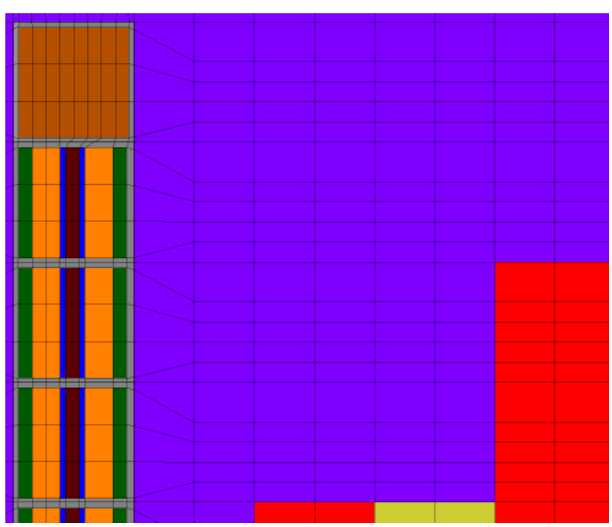

Figure 3.4. Spatial Heterogeneity for each drawer

As is the case with all deterministic transport calculations, a detailed space-angle-energy study is required for each model. There was insufficient time to complete the study for energy although we note that previous results indicate that the 70 group structure used here is reasonably accurate. In the case of this study, one has to be very careful about the increased

heterogeneity which should not require additional spatial modeling, but will require additional angular modeling. For each model, four meshes were built and several different cubature orders of the Legendre (L) – Tchebychev (T) product cubature were used along with changes to the anisotropic scattering approximation. Table 3.4 shows the details of the space-angle convergence for the k_{eff} results. With the exception of the calculations using the finest mesh, all of the other calculations utilized the coarsest mesh.

Table 3.4. k_{eff} Space-Angle Convergence for the Four Heterogeneous Models of Loading 104

	Model 1	Model 2	Model 3	Model 4
L7T7 P3	1.00131	1.00112	1.00090	1.00033
L7T7 P1	1.00096	1.00078	1.00056	0.99998
L3T7 P1	1.00096	1.00077	1.00054	0.99993
L15T7 P1	1.00097	1.00079	1.00057	1.00000
L3T3 P1	1.00094	1.00072	1.00043	0.99970
L3T15 P1	1.00098	1.00081	1.00061	1.00008
L3T31 P1	1.00098	1.00082	1.00063	1.00013
L3T3 P1 finest mesh	1.00098	1.00076	1.00049	0.99978

Starting with the spatial mesh refinement, one can see that there is only a slight improvement in k_{eff} even though this accounts for more than a factor of six improvement in the number of spatial vertices which is more or less expected with the SN2ND solver. The most dominate change in k_{eff} is observed when the anisotropic scattering order is increased from P_1 to P_3 and when the Tchebychev expansion is increased from T3 to T31 in the most heterogeneous model. Experience indicates that there is not much to be gained when using more than P_3 anisotropic scattering, but the angular approximation must be sufficiently converged to prevent substantial inaccuracies. In the case of model 4, it is likely that a T31 expansion in the Tchebychev cubature yields a converged k_{eff} because it uses twice the number of angles at T15. However, it is safe to assume that introducing heterogeneity will require cubature orders far higher than T31 if the observed trend in Table 3.4 continues.

Assuming the preceding results with respect to angle are near the linear point of asymptotic convergence, we can extrapolate the full space-angle convergence on the coarsest mesh and relatively low order angular approximation to the finest mesh and highest order angular approximation to obtain the results in Table 3.5. This extrapolation is necessary at this point because the old SN2ND solver is incapable of solving these problems combined with the memory constraints of BlueGene/P. It should not be unreasonable to assume that the extrapolated values in Table 3.5 are accurate to 10 pcm, but ideally these calculations will be redone with the new version of SN2ND when it becomes available. From Table 3.5, it is easy to see that the k_{eff} results are notably dropping as more heterogeneity is introduced into the model which is consistent with the observed errors in the heterogeneous model of ZPR-6/6A. Further study indicated that this was a fundamental bias in the heterogeneous cross section observable on a one-dimensional lattice cell. A two step cross section procedure does not appear wise in this scenario since the bias from each individual MC^2-3 cell calculation will be different.

Table 3.5. Extrapolated k_{eff} results for ZPR6/7 Loading 104

Experiment	1.00072 ± 0.00080
Monte Carlo	1.00016 ± 0.00007
Homogeneous	1.00149
Het. Model 1	1.00135
Het. Model 2	1.00124
Het. Model 3	1.00099
Het. Model 4	1.00067

Continuing with the foil reaction rate comparisons, the new results need to be compared with the results from the homogeneous model to determine if the heterogeneity causes degradation in the flux solution. Table 3.6 shows the foil results which indicate that the C/E results for a heterogeneous model are similar to those obtained using the homogeneous models. However, there appears to be a small increase in the error for EU fission and Pu49 fission in foil locations close to the central sodium channel. This was even more apparent in calculations for loading 120 which are not shown for brevity. This increased error is believed to be due to the foil cross section data rather than space-angle-energy inaccuracies from SN2ND and is left for the focus of future work.

Table 3.6. Loading 104 C/E Values in % Error for Normalized Foil Reaction Rates

Y	EU fission		DU capture		DU fission		Pu49 fission	
(cm)	Hom.	Het.	Hom.	Het.	Hom.	Het.	Hom.	Het.
3.53	2.60	3.22	-0.82	-0.37	1.25	0.05	2.92	3.15
4.55	2.62	2.67	0.58	0.58	-0.18	0.67	3.39	3.58
5.56	2.73	2.71	1.65	1.58	-0.34	0.93	3.03	3.27
6.58	2.84	2.97	1.79	1.86	0.42	0.71	3.01	3.22
7.60	2.61	3.12	0.48	0.87	1.33	0.00	2.40	2.62
9.06	2.29	2.82	0.53	0.94	2.01	0.44		
10.07	2.37	2.48	1.45	1.52	0.80	0.44	2.41	2.53
11.09	2.36	2.33	1.89	1.83	0.29	0.45	2.09	2.18
12.10	2.05	2.11	1.47	1.52	0.89	0.21		
13.12			0.59	0.93	2.20	0.04		
14.58			-1.19	-0.81	2.54	0.24		
15.60	1.43	1.53	0.91	0.99	1.16	0.18		
16.61	1.67	1.64	1.39	1.34	0.65	0.34	1.64	1.66
22.14	2.01	1.91	1.90	1.80	0.79	0.60	2.32	2.31
27.66	2.06	2.05	0.75	0.76	2.28	1.68	2.17	2.12
33.19	2.09	2.01	0.40	0.36	1.88	1.34	2.14	2.03
44.24	1.66	1.57	-0.94	-0.98	1.72	1.59	1.70	1.67
55.28	1.88	1.75	0.67	0.62	1.03	0.62	1.01	0.89
66.33	0.00	0.00	0.00	0.00	0.00	0.00	0.00	0.00

As mentioned, the preceding ZPR work is being done to validate the fast reactor homogeneous and heterogeneous modeling capability. The targeted capability is the

conventional two step procedure involving 1) MC^2-3 slab geometry models of important drawers to generate homogenized coarse group cross sections, and 2) SN2ND solutions incorporating the necessary space-angle + scattering order refinements of the homogenized problem. In most cases we observed relatively minor dependence on the space-angle-energy approximation incorporated in the SN2ND solver with most of the issues derived from the cross section generation methodology (i.e. step 1). This is not unexpected given the considerable experience with doing the two step procedure and simply points out that the transport solver in step 2 is not as important as the work done in step 1. The much less studied approach is to generate heterogeneous cross sections using a similar two step procedure. In this case, consistent error was traceable to the heterogeneous cross section data that requires more research to resolve.

3.3 Homogenized Assembly Modeling of the MONJU Fast Reactor

MONJU is a Japanese sodium-cooled fast reactor located in Tsuruga, Fukui Prefecture. MONJU is a demonstration plant for recycling and burning spent nuclear fuel from the fleet of light water reactors operating in Japan. The reactor first achieved criticality in April 1994 and it operated for a little over a year until a sodium leak, and a cover-up scandal, caused its shutdown until 2010. The reactor was restarted in May 2010 and during the following months numerous reactor physics measurements were made. While the core composition of MONJU is not precisely specified, with approximate compositions we can still produce good estimates of several key reactor physics parameters and thus extend the validation case for MC^2-3 + SN2ND. Combined with comparisons against experiments, these types of calculations help ensure confidence in the PROTEUS reactor physics tool being developed under NEAMS.

We used CUBIT [23] for generating the various meshes where the same hexagon meshing scheme was used for all hexagons in the core. Four spatial meshes of each assembly were created in these studies which are shown in Figure 3.5. Using these schemes, the total number of spatial vertices in the full core models were 322,530, 952,403, 2,658,351, and 4,210,574 which we denote as Model 1, 2, 3, and 4, respectively. Both 70 group and 230 group calculations were executed and the angular approximation was progressively increased from S_2 to S_8.

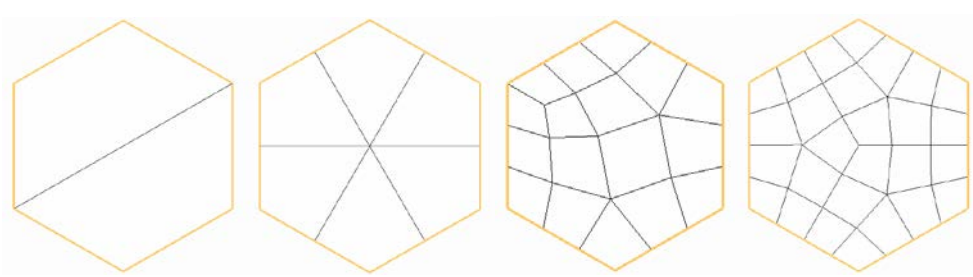

Model 1 Model 2 Model 3 Model 4

Figure 3.5. Finite Element Mesh per Hexagon for the SN2ND Models.

Tables 3.7 and 3.8 summarize eigenvalue results for various combinations of the spatial mesh and angular approximations in SN2ND on the fully inserted C1 configuration. Table 3.7 summarizes these results using 70-group cross sections while Table 3.8 does the same for a 230 group structure. Note that the memory limitations of BG/P combined with the old

SN2ND solver limits the number of 230-group calculations that can be performed. In these tables, empty positions correspond to runs that were not attempted while spaces with (**) indicate those cases that failed to run on BG/P because of the aforementioned memory limitations.

Table 3.7. UNIC Space-Angle Mesh Refinement using 70 Group Cross Sections

Angular Cubature	Scattering Order	Spatial Mesh			
		Model 1	Model 2	Model 3	Model 4
L1T1/S2	P1	0.98981	0.99010		0.99021
L3T3	P0	1.02762	1.02793		1.02804
	P1	0.99083	0.99115		0.99127
	P3	0.99166	0.99199	0.99209	0.99211
	P5	0.99165	0.99198		0.99211
S6	P3	0.99171	0.99205		0.99217
L5T5	P0	1.02765	1.02796		1.02808
	P1	0.99087	0.99120		0.99132
	P3	0.99173	0.99206		0.99219
S8	P3	0.99173	0.99207	0.99217	0.99220
	P5			0.99219	**

Table 3.8. UNIC Space-Angle Mesh Refinement using 230 Group Cross Sections

Angular Cubature	Scattering Order	Spatial Mesh			
		Model 1	Model 2	Model 3	Model 4
L1T1	P1	0.99008	0.99038		0.99049
L3T3	P1	0.99111	0.99143	0.99153	0.99155
L5T5	P1	0.99115	0.99147	**	**

From these tables, if we arbitrarily choose to judge a given space-angle approximation to be converged by requiring the change in eigenvalue to be less than 10 pcm when either the spatial mesh or the angular approximation is refined to the next available approximation, it can be seen that this convergence is achieved at the L3T3 angular approximation level for the Model 3 spatial mesh and with a P_3 scattering approximation. For this problem, the 230-group eigenvalue is expected to be ~0.99236 assuming it can be extrapolated from data in the above tables.

A more thorough analysis of convergence must include a comparison of group fluxes resulting from the use of different space-angle-energy approximations. To achieve this, 9-group fluxes were generated from 70 and 230 group calculations along the line ED shown in Figure 3.6 starting radially at point E in which the line intersects the domain and ending at point D where it exits the domain. The axial location of the line is such that, when C1 is fully inserted, it passes through the active parts of C-type control rods, C1, and approximately 10 cm below the B-type control rod.

Figure 3.7 shows the 9-group total fluxes across the edit line ED in the upper left picture which were integrated from a 230-group L3T3, Model 4 calculation using a P1 scattering order. The upper right picture in Figure 3.7 is the percent deviation of the 9 group fluxes of

the Model 3 mesh from the Model 4 mesh using a common S_8, 70 group data with a P_3 scattering order. It can be seen that all group flux errors are less than 1% except for the lowest energy group which from the upper left picture is 4-6 orders of magnitude less than the other group fluxes. The lower left picture in Figure 3.7 shows the percent deviation of the 9-group fluxes of L3T3 cubature from the L5T5 cubature using a common Model 4 mesh, 70 group data with P1 scattering.

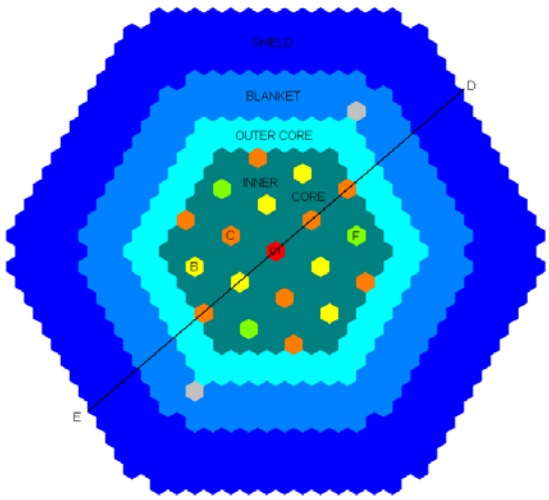

Figure 3.6. Schematic of the MONJU Reactor Showing the Edit Line ED.

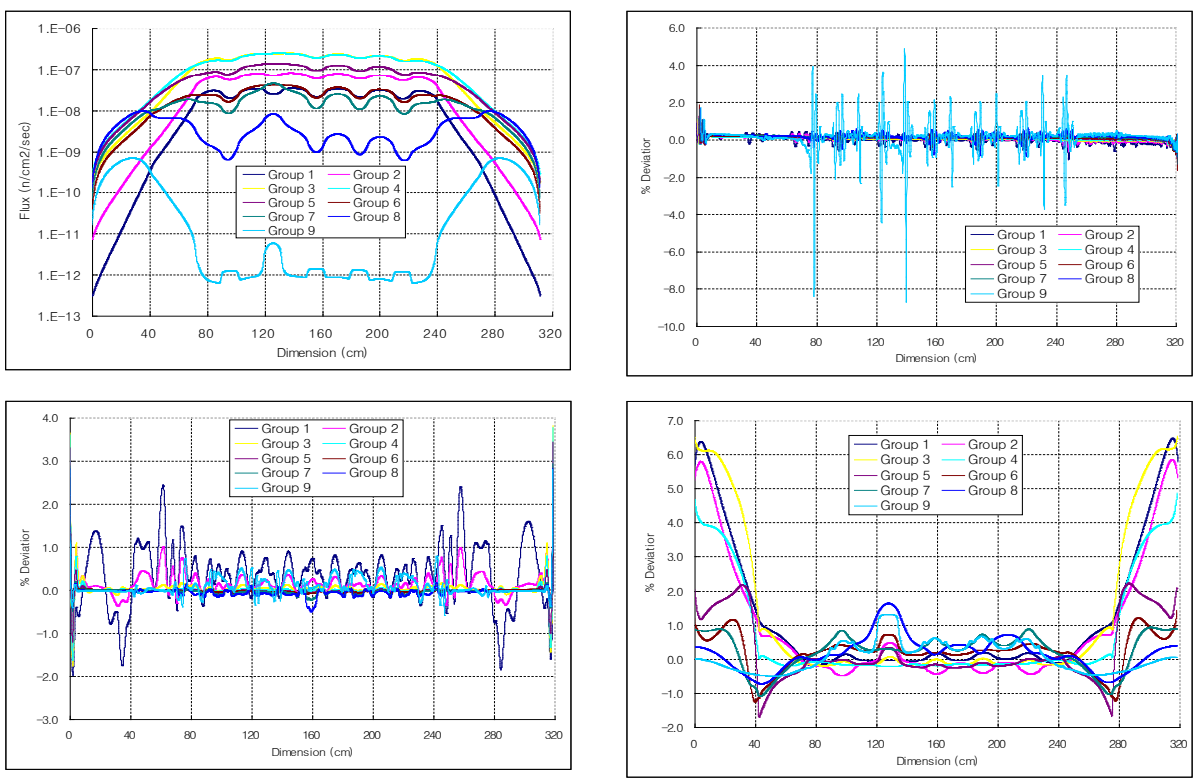

Figure 3.7. Nine Group Flux Edits on the Selected Line ED in Figure 3.6.

Again, most deviations are less than ~2% except at the domain boundaries where it is observed to increase to nearly 4%. After further inspection, a detailed comparison of the 70 group fluxes is much larger (up to 15%) which implies the need for higher angular approximation to eliminate the ray effects which dominate the errors observed in Figure 3.7. The lower right picture in Figure 3.7 shows the deviation of the 70 group from a 230 group calculation using a common Model 4, L3T3 cubature and P1 scattering order. In this case we observe much larger errors which appear in the radial blanket and shielding. In this case we know that it is a cross section issue, and a detailed flux comparison should be replaced with a reaction rate estimate such as iron capture. Nevertheless, the results are sufficient to indicate that 70 groups does not result in a fully converged solution (i.e. on the asymptotic plane of convergence for the numerical discretization), especially for cases where the magnitude of the fast flux is important (irradiation damage), and thus one should use a 230 group approximation when possible.

In addition to SN2ND, we can use the legacy tool VARIANT to obtain solutions to the MONJU problem. Table 3.9 summarizes 70-group, P3 scattering SN2ND and VARIANT eigenvalues for three configurations of the central control rod C1. In these calculations, the L3T3 cubature and a Model 3 mesh are used in SN2ND while two VARIANT calculations are provided corresponding to source-flux-leakage expansion orders of 661 and 461 and a P_5 angular spherical harmonics order. From Table 3.9 one can see there is a considerable difference of 90 pcm between SN2ND and VARIANT which has been traced to the difference in the way the fission spectrum (χ) is used in VARIANT and SN2ND. Also note that a full spatial convergence study of VARIANT (461 versus 661, etc.) is not done but that 661 is typically sufficient.

Table 3.10 gives the SN2ND and VARIANT estimates of the isothermal temperature coefficient of reactivity. It can be seen that the results show perfect agreement with the measured data, but the individual eigenvalues between VARIANT and UNIC are notably different which is consistent with the χ issue mentioned above. It is important to note that the VARIANT code cannot currently be used to solve ZPR drawer homogenized calculations and thus we cannot use as much validation data as we can with SN2ND.

Table 3.9. MONJU k_{eff} Results for Different Central Control Rod Configurations

Solution Method	Multiplication Factor		
	Critical Position	Fully Inserted C1	Fully Withdrawn C1
SN2ND	0.99927	0.99209	1.00201
VARIANT 661	1.00017	0.99302	1.00290
VARIANT 461	1.00032	0.99317	1.00306

Table 3.10. SN2ND and VARIANT Isothermal Temperature Coefficient for MONJU

	C1 withdrawal length (mm)	Multiplication Factor		Temperature Coefficient (%Δk/k/°C)	C/E
		195.7 °C	302.5 °C		
SN2ND	442	1.00021	0.99699	– 0.00302	1.003
VARIANT		1.00128	0.99808	– 0.00300	0.999
SN2ND	703	1.00347	1.00023	– 0.00303	1.004
VARIANT		1.00454	1.00132	– 0.00300	0.999

3.4 Fully Heterogeneous Modeling of Nuclear Reactors

In addition to the preceding validation work, we added a scoping study to determine the existing capability on fully heterogeneous reactor geometries. While DeCART is a much more practical tool than SN2ND for thermal reactor analysis at this time, determining the impact of trying to use a true three-dimensional geometry modeling capability versus a 2D-1D model is useful. A significant amount of time was spent building whole core heterogeneous models of several reactor geometries incorporating "representative" cross section data. The basic idea of course was to identify weaknesses in the existing SN2ND solver and provide guidance for the development of the new version of SN2ND (spatial multigrid).

The specific reactor types we considered are the Westinghouse pressurized water reactor (PWR), a proposed very high temperature reactor (VHTR), and the sodium cooled fast reactor MONJU. To begin we start with the PWR reactor which is graphically depicted in Figure 3.8.

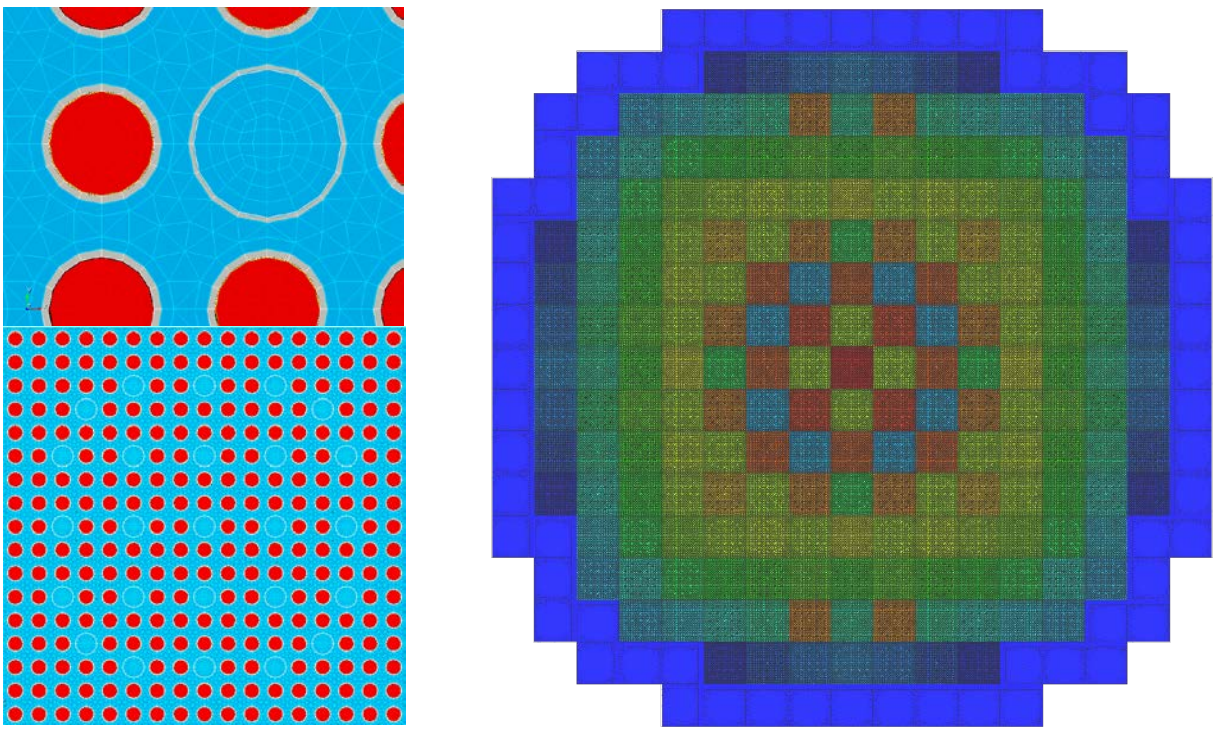

Figure 3.8. PWR Finite Element Meshed Geometry.

Figure 3.8 shows that there are a substantial number of finite elements in the model. The typical PWR modeling geometry is ~3.6 meters tall and ~3 meters in diameter and the simple two-dimensional representation shown in Figure 3.8 has over 2,000,000 finite elements. For a two-dimensional geometry with curvilinear finite elements, this will easily translate to tens of millions of vertices. During the attempts to obtain a solution for a three-dimensional calculation, PETSc was found to have a non-scaling memory operation (on BG/P) which restricts the overall mesh to have less than 35,000,000 total vertices. Given the stated radial mesh it should be rather obvious that any axial mesh would contain extremely bad aspect ratio elements; so much so that it rendered the system unsolvable. It is important to also note that two-dimensional solutions were also not obtainable in the old SN2ND solver because of the

high dominance ratio (proximity of the first two eigenvalues) in the eigenvalue/eigenvector system. The old version of SN2ND has a Tchebychev acceleration technique which proved insufficient hence the development of a Weilandt and/or restarted Arnoldi [14] process in the new version.

The next reactor problem is the VHTR which is shown in Figure 3.9. The VHTR is actually larger than the PWR, but the complexity is much lower because of the reduced number of fuel assemblies. Nevertheless, the PETSc issue also prevented us from solving the VHTR which was verified by making a non-physical small core height problem which could be solved. The mesh shown in Figure 3.9 has 2,500,079 elements in the two-dimensional plane and we easily need more than 100,000,000 elements because of the large axial dimensions (~8 meters).

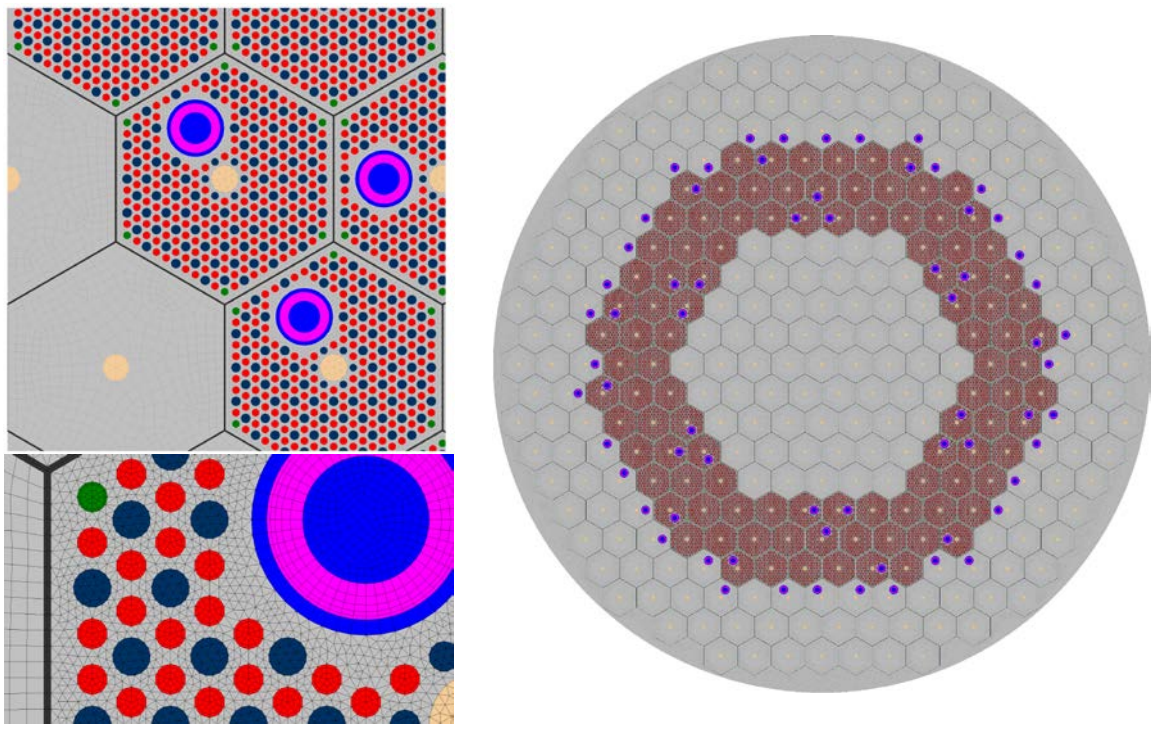

Figure 3.9. VHTR Finite Element Meshed Geometry.

The final whole core reactor model we attempted was the MONJU fast spectrum reactor shown in Figure 3.10. Compared with the preceding two reactor types, one can easily see that the MONJU reactor has comparable geometric detail with ~2.5 million elements to define a two-dimensional slice. However, the advantage of the fast spectrum system is that the core is less than a meter tall and removal of any upper and lower structural materials will not greatly change the solution (leakage is affected). While the change in geometry does negate the accuracy, we were able to obtain results with a mesh containing 45,477,696 elements and 30,069,349 vertices (used linear finite elements) combined with a 33 group cross section set and S_6 angular cubature. While the dominance ratio was high (0.6), the existing SN2ND solver algorithm is able to sufficiently accelerate the calculation. In effect, because a bulk of the effort in developing SN2ND has been focused on fast reactor problems, it should come as no surprise that it works well on fast reactor problems.

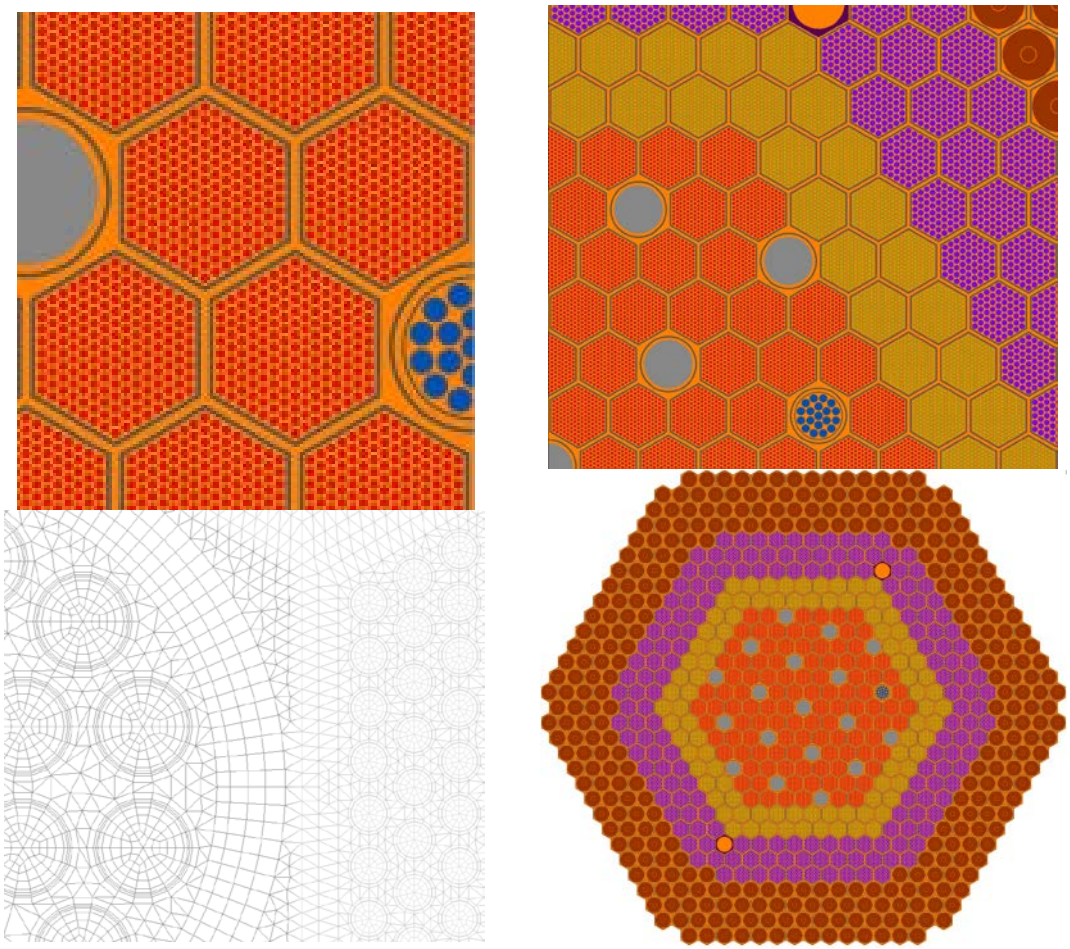

Figure 3.10. MONJU Finite Element Meshed Geometry

Figure 3.11 shows some more detail on the three dimensional geometry along with example flux and power solutions where we have split the geometry into lower shield (truncated size), lower blanket, lower core, upper core, upper blanket, upper plenum (truncated size). Note that a control rod was inserted into the core as seen in Figure 3.10 to cause a radial offset in the solution. This makes the problem more difficult and allows us to study spatial mesh convergence near the control rod since the flux solution typically goes negative near regions with insufficient mesh refinement.

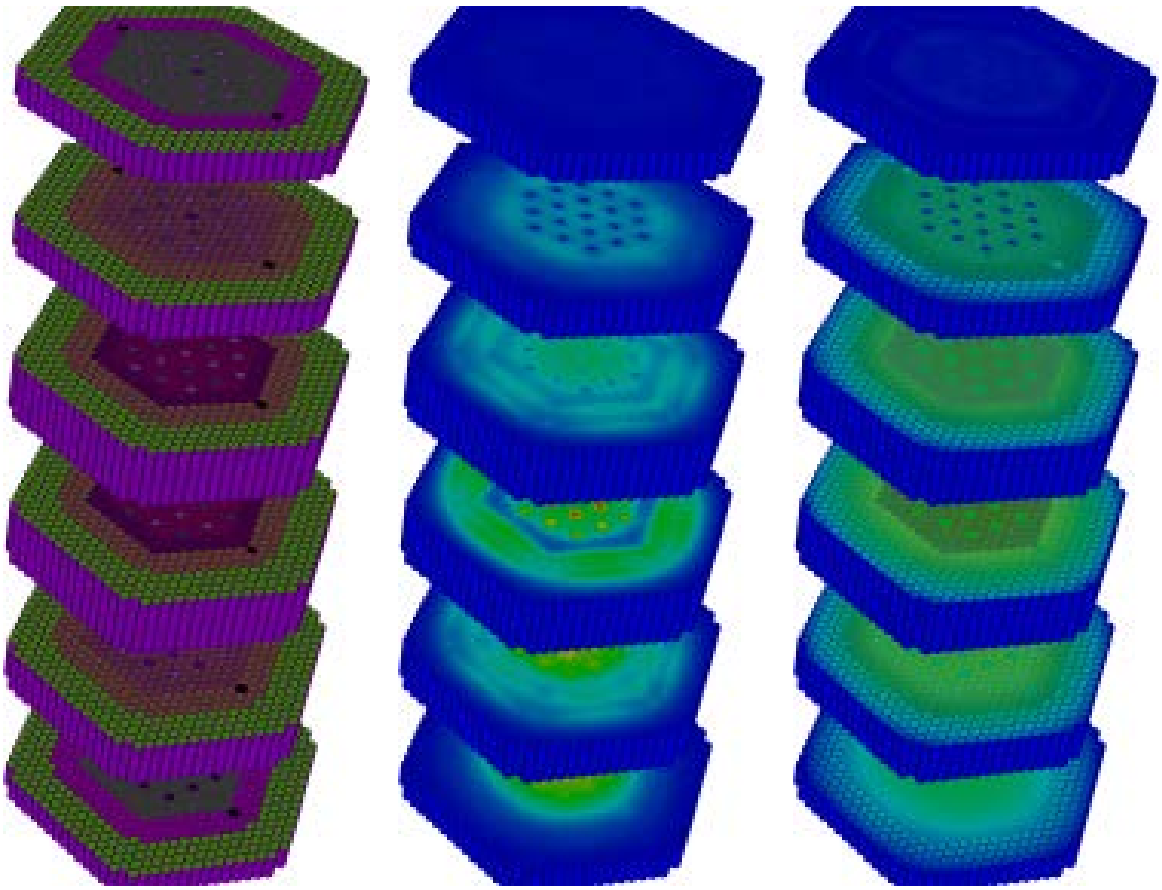

Geometry Group 23 Flux Power on Log Scale

Figure 3.11. MONJU 3D Geometry and Flux and Power Solutions

Overall, one fourth of the allocated time on BG/P time was spent running or attempting to run these large calculations. Numerous changes were made to the code to fix scalability issues that were external to PETSc such as the mesh import and cross section data loading. The non-scaling issue in PETSc which limited the preceding calculations is scheduled to be fixed in the next release.

4 Conclusions

Significant gains were made with regard to building the new SN2ND preconditioner and meeting the objectives of 1) parallelism in energy, 2) a spatial multigrid concept 3) using S_N vector spaces to accommodate the adjoint and time dependent functionalities needed for NEAMS work, and 4) complete manuals and documentation. While we failed to achieve the desired goal of an exportable SN2ND usable within the NEAMS community for neutronics analysis, we can be confident that this year's work puts the SN2ND solver well on its way to meeting that objective.

The old SN2ND solver used a Gauss-Siedel iterative algorithm in energy which is optimal for fast reactors. However, this iterative algorithm is not scalable and thus large calculations involving large numbers of energy groups but small numbers of space-angle vertices cannot fully utilize the available resources and typically over-run the system with regard to memory usage. A new solver algorithm using a GMRES solver over the entire space-angle-energy

system, both even- and odd-parity, was created and a preconditioner was built utilize spatial multigrid. The spatial multigrid technique was by far the most time consuming part of the development process because it required multiple new data structure concepts along with identifying the necessary changes in the vectors and their associated functions. As shown in this report, the tessellation introduces a known change in the odd-parity system of equations, the outcome of which is not known at this time, but must be assessed soon. Overall, the new coding is working in serial but clearly there is considerable work to be done to optimize the performance of the new preconditioner when parallelization in space, angle, and energy are applied.

In addition to code modifications, more work setting up validation problems for fast reactor analysis was done. A considerable amount of time was again spent setting up and performing ZPR calculations. This required additional auxiliary tool development much like that seen in previous years but not discussed in this report. Unlike previous work, FY2011 work included comparison of the solution against foil reaction rates taken during the experiments. Not only was a conventional homogenized drawer model attempted, but partially dehomogenized models were also constructed and tested. From this work it was clear that the homogenized drawer model produced excellent results for both the eigenvalue and foil measurements on four loadings of ZPR-6/7 although there was some notable room for improvement for the cross section generation scheme. The heterogeneous models of ZPR-6/7 also produced good results; however, a fundamental issue with the consistency of the cross section data indicates that the conventional two step procedure needs additional research when used for whole core heterogeneous calculations. The overall goal of these ZPR validation cases is to build a library of problems for PROTEUS that can be executed quickly when any changes are made to the individual components of PROTEUS.

In addition to the ZPR validation work, additional calculations were performed for more recent experimental data taken during the start-up tests of MONJU. Once again, MC^2-3 + SN2ND performed excellently for conventional homogeneous modeling and provided solutions that existing legacy codes could not. A detailed space-angle-energy analysis on both the eigenvalue and flux solution was carried out and discussed in this report. While the MONJU fuel compositions are not given, using reasonable estimates proved to yield accurate estimates of measured reactivity coefficients.

Mock-up heterogeneous calculations also took a considerable amount of time in FY2011. The purpose of these calculations is to scope out the performance limitations of SN2ND on whole core heterogeneous calculations. Specifically, heterogeneous PWR, VHTR, and MONJU reactor models were created using anywhere from 2 group to 33 group cross section data. As expected, meshes with greater than 100,000,000 vertices are necessary but cannot be achieved on existing super-computing machines with the current SN2ND solver. A specific non-scaling memory issue in PETSc actually prevented the SN2ND from being able to use an appropriate model of the PWR and VHTR (i.e. accurate dimensions). The PETSc related issue also affected the MONJU reactor, but since the active core height is so much shorter than the PWR and VHTR, we were still able to obtain a meaningful solution.

The current goals for SN2ND are to get the new version fully debugged with respect to space-angle-energy parallelism, reliable in execution, and to have comparable performance to the existing solver such that it can be released within the NEAMS community. After its export to RSICC, we will rely upon further preconditioner research to be done in collaboration with

university partners. One future area of research that appears most promising is to incorporate a multigrid step involving a structured grid overlay involving geometric homogenization of the detailed geometry. Additional work will be focused on making SN2ND applicable on thermal reactor problems and addressing the concerns with handling void regions.

5 References

1. A. Siegel, T. Tautges, A. Caceres, D. Kaushik, and P. Fischer, "Software Design of SHARP," *Proc. Joint Int'l Topical Mtg. on Mathematics & Computation and Supercomputing in Nuclear Applications*, Monterey, California, April 15–19, 2007.
2. M. A. Smith, A. Mohamed, A. Marin-Lafleche, E. E. Lewis, K. Derstine, C. H. Lee, A. Wollaber and W. S. Yang. FY2010 Status Report on Advanced Neutronics Modeling and Validation, ANL-GenIV-149, Sept. 2010.
3. Micheal A. Smith, Dinesh Kaushik, Allan Wollaber, Won Sik Yang, Barry Smith, Cristian Rabiti, Giuseppe Palmiotti, "Recent Research Progress on UNIC at Argonne National Laboratory," International Conference on Mathematics, Computational Methods & Reactor Physics, Saratoga Springs, New York, May 3-7, 2009.
4. D.P. Weber et al, "High Fidelity LWR Analysis with the Numerical Nuclear Reactor," Nuclear Science and Engineering, **155**, 395-408 (2007).
5. M. A. Smith, A. Mohamed, C. H. Lee, A. Marin-Lafleche, and W. S. Yang, "Zero Power Fast Reactor Deterministic Modeling with Heterogeneous Geometry," Trans. Am. Nucl. Soc., Hollywood, FL, USA, June 26-30, 2011.
6. B. J. Toppel, H. Henryson II, and C. G. Stenberg, "ETOE-2/MC2-2/SDX Multi-group Cross-Section Processing," Conf-780334-5, Presentation at RSIC Seminar Workshop on Multi-group Cross Sections, Oak Ridge, TN, March 1978.
7. G. Palmiotti, E. E. Lewis & C. B. Carrico, "VARIANT: VARIational Anisotropic Nodal Transport for Multidimensional Cartesian and Hexagonal Geometry Calculation," Argonne National Laboratory ANL-95/40, 1995.
8. Derstine, K. L., "DIF3D: A Code to Solve One-, Two-, and Three-Dimensional Diffusion Theory Problems," ANL-82-64, Argonne National Laboratory.1982.
9. S. Balay, K. R. Buschelman, W. D. Gropp, D. K. Kaushik, M. G. Knepley, L. C. McInnes, and B. F. Smith, "PETSc home page," www.mcs.anl.gov/petsc.
10. Personal Communication, Tom Manteuffel, Allan Wollaber, Micheal A Smith, et. al., University of Colorado at Boulder, October 2009.
11. Yair Shapira, "'Algebraic multigrid,' Matrix-based multigrid: theory and applications." Springer. ISBN 1402074859 (2003).
12. Y. Saad and M.H. Schultz, "GMRES: A generalized minimal residual algorithm for solving nonsymmetric linear systems", SIAM J. Sci. Stat. Comput., **7**:856-869, 1986.
13. Y. Saad, Iterative Methods for sparse Linear Systems, 2nd Ed. SIAM, Philadelphia, 2003
14. W. E. Arnoldi, "The Principle of Minimized Iteration in the Solution of the Matrix Eigenvalue Problem," Quart. Appl. Math. 9 17-29 (1951).
15. Personal Communication, Richard M. Lell and Micheal A Smith, Argonne National Laboratory, January 2009.

16. NEA Nuclear Science Committee, "International Handbook of Evaluated Criticality Safety Benchmark Experiments," NEA/NSC/DOC(95)03, September 2007.

17. Richard M. Lell, James A. Morman, Robert W. Schaefer and Richard D. McKnight, "ZPR-6 Assembly 7 High ^{240}Pu Core Experiments: A Fast Reactor Core With Mixed (Pu,U)-Oxide Fuel and a Central High ^{240}Pu Zone." ZPR-LMFR-EXP-002, CRIT-REAC-RRATE, NEA/NSC/DOC(1006)1.

18. W. R. Robinson and G. S. Stanford, "Effect of Simulated B_4C Control Rods on Reaction Rate Distribution in Assembly 7 with the High 240 Plutonium Zone," ZPR-TM-74, Argonne National Laboratory, 1971.

19. Oak Ridge National Laboratory, The Radiation Safety Informational Computer Center, "RSICC web page," http://www-rsicc.ornl.gov/.

20. Argonne National Laboratory, Argonne Leadership Computing Facility, http://www.alcf.anl.gov.

21. VisIt. Website, Lawrence Livermore National Laboratory. http://www.llnl.gov/visit.

22. J. F. Briesmeister, et al., "MCNP – A General Monte Carlo N-Particle Transport Code, Version 5, User's Guide, Volume II", Los Alamos National Laboratory, LA-UR-03-0245, October 2005.

23. T. D. Blacker and et al. CUBIT mesh generation environment, Volume 1: Users manual. Sandia National Laboratory, 1994.

Nuclear Engineering Division
Argonne National Laboratory
9700 South Case Avenue, Bldg. 208
Argonne, IL 60439

www.anl.gov